Metrologia

REVIEW • **OPEN ACCESS**

Practical realisation of the kelvin by Johnson noise thermometry

OPEN ACCESS
IOP Publishing | Bureau International des Poids et Mesures Metrologia
Metrologia **61** (2024) 022001 (23pp) https://doi.org/10.1088/1681-7575/ad2273

Review

Practical realisation of the kelvin by Johnson noise thermometry

Samuel P Benz[1], Kevin J Coakley[1], Nathan E Flowers-Jacobs[1], Horst Rogalla[1], Weston L Tew[2], Jifeng Qu[3], D Rod White[4,*], Christof Gaiser[5], Alessio Pollarolo[6] and Chiharu Urano[7]

[1] National Institute of Standards and Technology, Boulder, CO 80305, United States of America
[2] National Institute of Standards and Technology, Gaithersburg, MD 20899, United States of America
[3] National Institute of Metrology (NIM), Beijing 100029, People's Republic of China
[4] Independent Researcher, Lower Hutt, New Zealand
[5] Physikalisch-Technische Bundesanstalt (PTB), Berlin, Germany
[6] Measurements International (MI), Prescott, Canada
[7] National Metrology Institute of Japan (NMIJ), AIST, Tsukuba, Japan

E-mail: rodwhitenz@gmail.com

Received 9 November 2023, revised 13 January 2024
Accepted for publication 25 January 2024
Published 15 February 2024

Abstract

Johnson noise thermometry (JNT) is a purely electronic method of thermodynamic thermometry. In primary JNT, the temperature is inferred from a comparison of the Johnson noise voltage of a resistor at the unknown temperature with a pseudo-random noise synthesized by a quantum-based voltage-noise source (QVNS). The advantages of the method are that it relies entirely on electronic measurements, and it can be used over a wide range of temperatures due to the ability of the QVNS to generate programmable, scalable, and accurate reference signals. The disadvantages are the requirement of cryogenic operation of the QVNS, the need to match the frequency responses of the leads of the sense resistor and the QVNS, and long measurement times. This review collates advice on current best practice for a primary JNT based on the switched correlator and QVNS. The method achieves an uncertainty of about 1 mK near 300 K and is suited to operation between 4 K and 1000 K.

Keywords: Johnson noise, thermodynamic temperature, thermometry, international system of units, Josephson effect, Mise en Pratique for the kelvin

1. Introduction

On 20 May 2019, the General Conference on Weights and Measures promulgated a revision of the SI replacing the definitions of the kelvin, the ampere, the kilogram, and the mole with definitions based on fundamental physical constants [1]. The former SI definition of the kelvin, based on the triple point of water (TPW), was replaced by a defined value of the Boltzmann constant, $k = 1.380\ 649 \times 10^{-23}$ J K^{-1}. The redefinition has two significant benefits for thermometry. Firstly, whereas the uncertainty in the old kelvin definition was determined by the uncertainties in the practical realisation of the TPW of about 30 µK [2–4], the uncertainty in the new definition is zero, thus eliminating any intrinsic constraint on the uncertainty of practical realisations. Secondly, the old definition required a primary thermometer to perform well at both the TPW and the unknown temperature. This requirement rules out primary thermometers with a low sensitivity at the TPW, including all forms of radiation thermometer, and thermometers with material limitations at the TPW, including those relying on superconducting devices. With the

* Author to whom any correspondence should be addressed.

new definition, any temperature may be measured using any equation of state, using any technology, without reference to any other temperature.

The Consultative Committee for Thermometry currently recognises five types of primary thermometer capable of yielding uncertainties close to the state of the art [5], namely, acoustic-gas thermometry [6], spectral-band radiation thermometry [7, 8], dielectric constant gas thermometry [9], refractive index gas thermometry [10], and Johnson noise thermometry (JNT). JNT is the only purely electronic method, with the advantages of using a single well-understood technology and being less affected by uncertainties associated with non-ideal material properties (e.g. gases and blackbodies).

Noise thermometry has been investigated for a wide range of industrial and metrological applications spanning temperatures from below 100 nK to above 2500 K (for a recent review see [11]). However, the low signal levels characteristic of noise thermometry and the stochastic nature of the signal make the measurements very challenging. Historically, JNT has been considered practical only for installations where conventional temperature sensors are unable to be retrieved for recalibration, such as in nuclear reactors or satellites [11].

Beginning in the 1980s, with the advent of fast analog-to-digital converters (ADCs) and digital signal processing, JNT began to be considered for metrological applications [12–14]. For cryogenic applications, JNT was made practical by the development of superconducting quantum interference devices, which improved the signal-to-noise ratios of the measurement electronics by many orders of magnitude [15]. Primary cryogenic JNT is discussed in [16]. At higher temperatures, JNT with millikelvin accuracy was made practical by the development at the National Institute of Standards and Technology (NIST USA) of the Josephson arbitrary waveform synthesiser [17–21]. For JNT, the synthesiser is operated as a broadband quantum-based voltage-noise source (QVNS), enabling a significant increase in bandwidth of the noise thermometer with a corresponding reduction in the uncertainty. The development of the QVNS culminated in the 2017 Boltzmann constant determination at National Institute of Metrology (NIM China), which achieved a relative uncertainty of 2.7×10^{-6} [22] and contributed to the special adjustment of the fundamental constants [23] by the Committee on Data of the International Science Council (CODATA) prior to the redefinition of the kelvin. Similar state-of-the-art JNT measurements of k were completed at NIST and the National Metrology Institute of Japan (NMIJ Japan) and achieved, respectively, relative uncertainties of 5.0×10^{-6} [20, 21] and 1.0×10^{-5} [24].

This review collates advice on the best practice for JNT using a QVNS in combination with a switched correlator with the expectation of applications in the range from ∼4 K to ∼1000 K. In particular, the paper highlights key aspects of design and operation that may not have been apparent in previous publications. Section 2 outlines the basic principles of JNT including the equation of state, noise-power measurement with the switched correlator, absolute and relative primary JNT, and explains the importance of frequency-domain data processing. Section 3 discusses each of the main building blocks of the JNT highlighting important design constraints and sources of measurement error. Section 4 discusses the use of cross validation (CV) for the data analysis; an important technique that eliminates the need for subjective assessments of residual systematic effects. Section 5 then compiles uncertainty budgets based on two sets of experiments. The first is the set of Boltzmann constant determinations undertaken at NIM and NIST at the water triple point (WTP, 273.15 K). The second set is the collection of T–T_{90} determinations undertaken at NIST between 500 K and 800 K. The review closes with a summary of conclusions and suggestions for further research.

2. Basic measurement principles

This section outlines the basic principles of JNT as applied to the measurement of thermodynamic temperature, including the equation of state, noise-power measurement with the switched correlator and QVNS, noise-power measurement statistics, absolute and relative primary JNT, and the importance of frequency-domain data processing.

2.1. Foundation

Johnson noise is the electronic noise caused by the random thermal motion of charge carriers occurring within all electrical conductors. Johnson noise, sometimes called Nyquist noise, is named after J B Johnson who was the first to make definitive measurements of the noise in 1927 [25]. A second paper by Johnson a year later was accompanied by a paper by H. Nyquist deriving the equation relating the noise voltage to temperature [26, 27]. Although the discovery of the noise is generally attributed to Johnson and Nyquist, in fact, the noise was predicted by Einstein in his 1905 explanation of Brownian motion [28], more than two decades earlier.

Johnson noise and Brownian motion are just two examples of phenomena where the microscopic random thermal motions of charges, atoms, or molecules give rise to macroscopic dissipative effects (electrical resistance and viscosity in these cases). The fluctuation–dissipation theorem developed in 1951 by Callen and Welton [29] (see also [30]) explains why similar noise phenomena occur in all linear dissipative systems.

For Johnson noise, the fluctuation–dissipation theorem relates the power spectral density (PSD) of the noise voltage across a conductor in terms of the real part of the conductor impedance, Re(Z), and its temperature, T,

$$S(f) = 4\,\mathrm{Re}(Z)\,\frac{hf}{\exp(hf/kT) - 1}, \tag{1}$$

where h is Planck's constant, f is frequency, and k is the Boltzmann constant. This expression, derived by Nyquist in the 1928 paper, is the one-dimensional form of the Planck blackbody law [31]. A term representing the quantum mechanical zero-point energy is often included in (1), however, its inclusion is controversial [32–34] as it causes the integral of the noise power over all frequencies to be unbounded. The most recent view, supported by experiment and analogy with

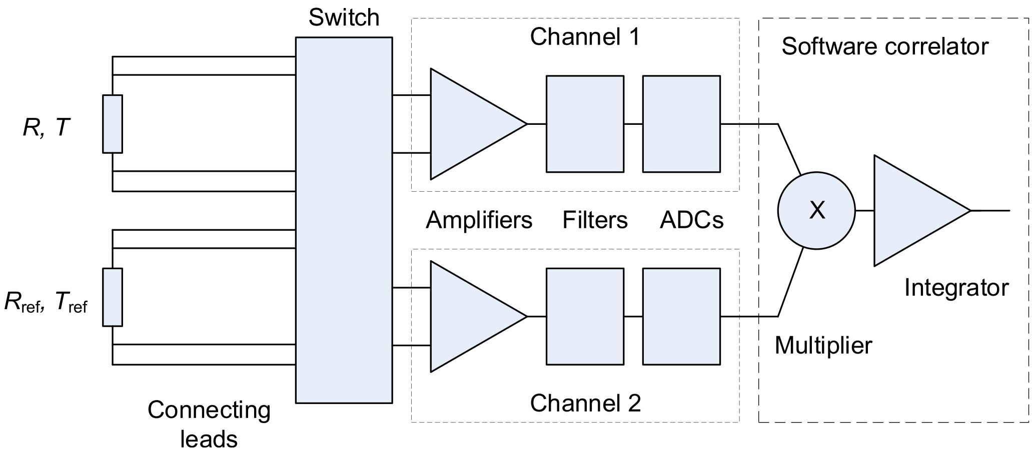

Figure 1. A simplified schematic diagram of a switched-correlator Johnson noise thermometer.

the Casimir effect [35], is that the term is not manifest in mechanically stable macroscopic systems and should be omitted. The contribution of the disputed term is negligible for all practical noise thermometry considered to date.

Johnson noise is usually characterized by its mean-square voltage, conventionally called the noise power. For temperatures above 25 K and frequencies below 1 MHz, the noise power is approximated with a relative error of less than 1×10^{-6} by Nyquist's law,

$$\left\langle V_T^2 \right\rangle = 4kT\mathrm{Re}\left(Z\right)\Delta f, \tag{2}$$

where Δf is the bandwidth over which the noise is measured. If a sensor is a pure resistance, R, the PSD $S(f) = 4kTR$ is independent of frequency, and the noise is described as 'white'. The noise voltage is small. A convenient rule of thumb is that the spectral density of the noise from a 1 kΩ resistor at room temperature is approximately 4 nV/$\sqrt{}$Hz, and when integrated over a 1 MHz bandwidth, the noise totals just 4 µV rms.

At high frequencies and low temperatures, Nyquist's law may not be a satisfactory approximation of (1). The relative error in (2) is given by the series expansion of the Planck factor

$$\frac{(hf/kT)}{\exp\left(hf/kT\right) - 1} = 1 - \frac{hf}{2kT} + \ldots \approx 1 - 2.4 \times 10^{-11}\frac{f}{T}, \tag{3}$$

so that a JNT using Nyquist's law near 1 mK and with an average operating frequency of 100 kHz is accurate to about 0.24%.

Note the notation used in (2); the bracket notation, $\langle \ldots \rangle$, indicates the expectation or theoretical value for a variate. The overscore symbol, $\overline{\ldots}$, (see (5) below) indicates a measured average, and the hat symbol (as in $\hat{T}$ in (5)) indicates a value estimated from measurement. The overscore symbol is used for both time averages and ensemble averages. Throughout the text, uncertainties are standard uncertainties, and relative uncertainties are expressed as parts per million (ppm).

2.2. The switched correlator

The switched-correlator noise thermometer, first developed by Brixy for use in the nuclear industry [36, 37], is currently the basis of all high-accuracy noise thermometers used above cryogenic temperatures and for metrological applications. It is a hybrid of the switched-rectifier radiometer developed by Dicke [31] and the cross-correlator developed by Fink [38]. Figure 1 shows a simple schematic diagram of a typical switched-correlator JNT, comprising a pair of resistor sensors, a switch connecting low-noise preamplifiers to one of the two resistors, a pair of amplifier chains including bandpass filters and ADCs, and a software multiplier and integrator. In most noise thermometers, the amplitude of the Johnson noise from the sense resistors is less than 1 µV rms necessitating voltage gains exceeding 100 000 through the amplifier chain to the ADC.

The purpose of the correlator is to eliminate systematic errors due to extraneous noise voltages generated within the amplifiers and the lead resistances to the sensors. If the input voltages to the two channels of the correlator are respectively $V_1 = V_T + V_{n2} + R_T(I_{n1} + I_{n2})$ and $V_2 = V_T + V_{n2} + R_T(I_{n1} + I_{n2})$, where V_{ni} and I_{ni} (with $i = 1, 2$) are respectively the equivalent input-noise voltages and input-noise currents of the two amplifiers (including the noise due to lead resistances), and V_T is the noise voltage produced by the sense resistor, R_T, then the average output of the correlator is proportional to

$$\langle V_1 V_2\rangle = \langle V_T^2\rangle + R_T^2\left[\langle I_{n1}^2\rangle + \langle I_{n2}^2\rangle\right] + R_T\left[\langle V_{n1} I_{n1}\rangle + \langle V_{n2} I_{n2}\rangle\right], \tag{4}$$

so that the output is the mean noise power, as given by Nyquist's law, with (typically) small errors due to the input-noise currents of the amplifiers. Figure 1 also shows the correlator has a natural four-wire definition of the sensor resistance, which eliminates lead resistance errors in measurements of the resistance, as well as errors in the noise power measurements due to uncorrelated noise generated in the leads.

Because the gain and bandwidth of noise thermometers are difficult to measure with sufficient accuracy, it is usual to make two measurements, one with the resistor at the unknown temperature, and another with a second resistor at a reference temperature. The unknown temperature is then estimated from the ratio of the measured noise powers, ideally independent of the gain and frequency response of the correlator:

$$\hat{T} = T_{\text{ref}} \frac{\overline{V_T^2}}{\overline{V_{\text{ref}}^2}} \frac{R_{\text{ref}}}{R_T}, \tag{5}$$

where T_{ref}, R_{ref}, and $\overline{V_{\text{ref}}^2}$ are respectively the temperature, resistance, and the measured average noise power of the reference resistor, and R_T and $\overline{V_T^2}$ are the resistance and measured average noise power of the resistor at the unknown temperature. Frequent switching between the two noise sources ensures that the measured ratio of the noise powers is unaffected by drifts in the gain and frequency response of the thermometer.

2.3. Noise statistics

Johnson noise is distributed normally with zero mean, so has the probability density,

$$p(V) = \frac{1}{\sqrt{2\pi \langle V_T^2 \rangle}} \exp\left(\frac{-V^2}{2\langle V_T^2 \rangle}\right). \tag{6}$$

In the absence of extraneous noise, a single sample of the noise power has a chi-square distribution with a single degree of freedom, a mean $\langle V_T^2 \rangle$, and a variance $2\langle V_T^2 \rangle$. If N statistically independent samples are averaged, then the mean-square voltage is distributed as a chi-square variate with N degrees of freedom, and the relative uncertainty in the measured noise power is given by

$$\frac{u^2\left(\overline{V_T^2}\right)}{\langle V_T^2 \rangle^2} = \frac{\left\langle \left(\overline{V_T^2} - \langle V_T^2 \rangle\right)^2 \right\rangle}{\langle V_T^2 \rangle^2} = \frac{2}{N}. \tag{7}$$

Further, if the JNT passband is rectangular with a bandwidth Δf, and the rectified voltage is sampled uniformly for a measurement period τ according to the Shannon sampling theorem, so that the number of statistically independent measurements is $N = 2\tau\Delta f$, the relative uncertainty in the noise power measurement can be expressed in terms of the thermometer bandwidth and the averaging time according to Rice's formula [39]:

$$\frac{u^2\left(\overline{V_T^2}\right)}{\langle V_T^2 \rangle^2} = \frac{1}{\tau \Delta f}. \tag{8}$$

Note that equations (7) and (8) apply only when a square-law rectifier is used. If a linear rectifier (or any other rectifier) is used, the measurement is less statistically efficient, and the relative uncertainty is higher [40].

Where the bandwidth of a thermometer is defined by analogue filters yielding a non-rectangular passband with a frequency response, $G(f)$, the effective bandwidth for calculating the relative uncertainty, (8), is the correlation bandwidth [31, 41–43],

$$\Delta f_{\text{c}} = \frac{\left[\int_0^\infty |G(f)|^2 \mathrm{d}f\right]^2}{\int_0^\infty |G(f)|^4 \mathrm{d}f}. \tag{9}$$

Equation (9) is a form of the Welch–Satterthwaite formula for the equivalent degrees of freedom [44] for linear combinations of variances, so that $2\Delta f_{\text{c}}$ is the effective number of degrees of freedom acquired per second by the thermometer.

Equation (8) gives the minimum uncertainty for the measurement of a noise power. When making temperature ratio measurements according to (5), two noise-power measurements are made, which doubles both the measurement time and the variance, so that the minimum relative uncertainty in a measurement of the unknown temperature is

$$\left.\frac{u\left(\hat{T}\right)}{T}\right|_{\min} = \left(\frac{4}{\tau_{\text{I}} \Delta f_{\text{c}}}\right)^{1/2} = \left(\frac{8}{N_{\min}}\right)^{1/2}. \tag{10}$$

Where $\tau_{\text{I}} = 2\tau$ is the total measurement time, and $N_{\min}$ is the minimum number of statistically independent samples required to achieve the relative uncertainty. For a measurement requiring a relative uncertainty of 0.001%, the minimum number of statistically independent samples is about 10^{11}. If the measurements are acquired at 100 kHz, the measurement time is more than 11 d.

In all measurements, there is additional uncertainty due to amplifier noise. The relative uncertainty in the temperature determination with the additional amplifier noise voltages, V_{n1} and V_{n2}, in each channel of the correlator is [43, 45]

$$\frac{u^2(\hat{T})}{T^2} = \frac{2}{\tau \Delta f_{\text{c}}}\left[\left(1 + \frac{\langle V_{\text{n1}}^2 \rangle}{\langle V_T^2 \rangle}\right)\left(1 + \frac{\langle V_{\text{n2}}^2 \rangle}{\langle V_T^2 \rangle}\right) + 1\right]. \tag{11}$$

The statistical uncertainty described by (11) is usually the single largest contribution to the total uncertainty in the measured temperature. Figure 2 plots the relative increase in variance due to amplifier noise (ratio of (11) to (10)), versus the noise-to-signal ratio, $\langle V_n^2 \rangle / \langle V_T^2 \rangle$ with $\langle V_n^2 \rangle = \langle V_{n1}^2 \rangle = \langle V_{n2}^2 \rangle$, and shows the importance of keeping the noise-to-signal ratio below 1.0. For noise-to-signal ratios below 1.0, the uncertainty in the measured noise power is dominated by the variance of the thermal noise signal, whereas for ratios above 1.0, the uncertainty is dominated by the variance of the amplifier noise.

2.4. Relative primary noise thermometry

Relative primary thermometers are those determining an unknown temperature as a ratio with respect to a known temperature, as described by (5). In this mode, both noise sources of figure 1 are resistors maintained at temperatures of interest; one at the known reference temperature, T_{ref}, the other, the

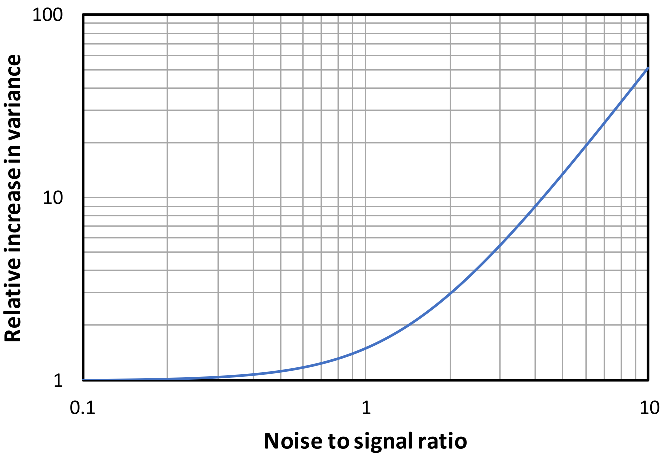

Figure 2. The effect of amplifier noise on measurement uncertainty.

measured temperature, T. Usually, the reference temperature is realised as a fixed point, often the TPW.

Relative primary noise thermometers generally have a restricted bandwidth and are therefore slower and have higher uncertainties than obtainable with absolute primary noise thermometers. The restriction in bandwidth arises from a conflict between two matching criteria. First, the effects of non-linearities in the electronics of the noise thermometer are minimised when the two noise sources produce noise of the same amplitude (see section 5.1.4 for details), that is,

$$R_T T \approx R_{\mathrm{ref}} T_{\mathrm{ref}}. \tag{12}$$

The second criterion arises from the need to match the frequency response of the connecting leads to the two sense resistors in combination with the preamplifier input capacitance, C_{in}. For short connecting leads, a first-order match of the frequency response is obtained if

$$R_T C_{\mathrm{in}} \approx R_{\mathrm{ref}} C_{\mathrm{in}}, \tag{13}$$

that is, the two resistances must be the same. Equations (12) and (13) cannot be satisfied at the same time, and some compromises must be made.

There are several approaches to managing the conflict, but none work well. The most common approach is to match the noise powers and operate the thermometer with a restricted bandwidth to minimise differences in the frequency response e.g. [46–48]. A second approach is to add trimming capacitors to the connecting leads for one of the switch positions so the time constants for the two sensors are the same [49]. This option enables some improvements in bandwidth, but the inductance of the connecting leads can make the option unworkable [50]. Thirdly, the thermometer can be operated over two frequency bands and a correction applied to account for the different responses within the two bands [51], but this, too, unreasonably assumes a simple model of the two frequency responses.

Examples of metrological applications of relative primary thermometers include measurements of the vapour pressure of helium near 4 K [45], measurements of thermodynamic temperatures of fixed points [52–54], and characterisation of molybdenum resistance thermometers [55]. Note that the relative measurements reported by Tew *et al* at NIST [56, 57] of temperatures up to the zinc point (~693 K), were made with an absolute primary thermometer, to be described shortly, operated in relative mode.

2.5. Absolute primary noise thermometry

Absolute primary thermometers are those that determine the unknown temperature without reference to another known temperature. In this mode, the resistor providing the reference noise signal is replaced by a synthetic-noise source producing a noise with a PSD calculable in terms of quantum-based electrical standards, as shown schematically in figure 3.

The PSD of the noise from a resistor at an unknown temperature, T, can be expressed as

$$S_R = 4kTX_R R_{\mathrm{K}}, \tag{14}$$

where the resistance is expressed as the ratio X_R in units of the von Klitzing resistance $R_{\mathrm{K}} \equiv h/e^2$, where e is the charge of the electron, and h is Planck's constant.

In the NIST and NIM noise thermometers, the reference noise source, the QVNS [17–19, 22, 58–63], produces a pseudo-random noise with an average PSD,

$$S_Q = D^2 N_{\mathrm{J}}^2 f_{\mathrm{s}} M / K_{\mathrm{J}}^2, \tag{15}$$

where $K_{\mathrm{J}} \equiv 2e/h$, is the Josephson constant, f_{s} is a clock frequency, M is the bit length of the digital code for the noise waveform (see section 3.2 below), D is an adjustable parameter of the software that generates the digital code and sets the amplitude of the synthesized waveform, and N_{J} is the number of junctions in the Josephson array used in the QVNS. As with relative noise thermometry, the thermometer is normally operated with the PSDs closely matched, $S_Q \approx S_R$. The unknown temperature is then determined as

$$\hat{T} = h \frac{D^2 N_{\mathrm{J}}^2 f_{\mathrm{s}} M}{16 k X_R} \frac{\hat{S}_R}{\hat{S}_Q} \tag{16}$$

where $\hat{S}_R/\hat{S}_Q$ is the estimated ratio of the PSDs inferred from measurements of the noise-power ratios, $\overline{V_R^2}/\overline{V_Q^2}$, made over a wide frequency range (see section 4 for detail). Since h and k are now defined without uncertainty, the parameters D, N_{J}, and M are software or hardware constants with zero uncertainty, and the sampling frequency f_{s} and the resistance ratio X_R can be measured with negligible uncertainty, the uncertainty in the measured temperature is almost entirely determined by the uncertainty in the estimate of the PSD ratio $\hat{S}_R/\hat{S}_Q$.

Because the QVNS produces a deterministic pseudo-random noise, the statistical uncertainty in the measurement of the QVNS noise power is less than for the thermal noise-power measurements [43]:

$$\frac{u^2\left(\overline{V_Q^2}\right)}{\left\langle V_T^2\right\rangle^2} = \frac{1}{2\,\tau\,\Delta f_{\mathrm{c}}}\left[\left(1+\frac{\left\langle V_{n1}^2\right\rangle}{\left\langle V_T^2\right\rangle}\right)\left(1+\frac{\left\langle V_{n2}^2\right\rangle}{\left\langle V_T^2\right\rangle}\right)-1\right]. \tag{17}$$

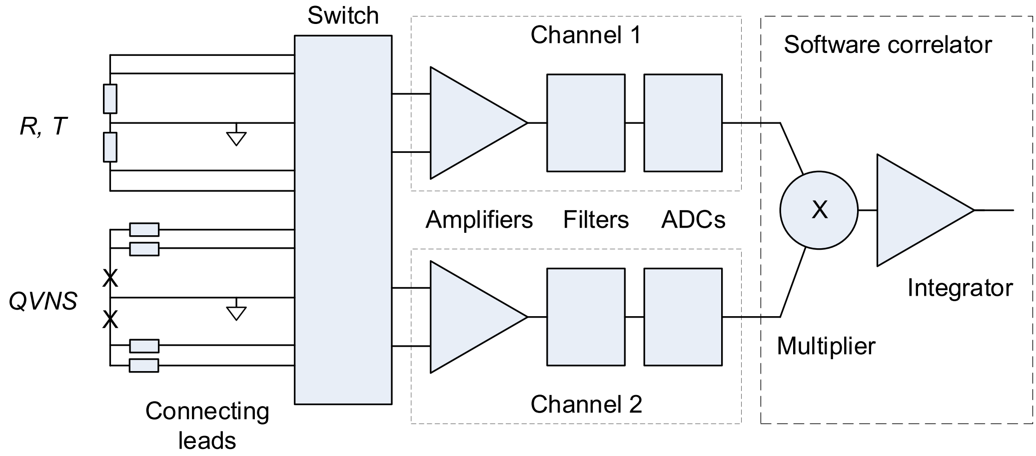

Figure 3. Block diagram of an absolute primary noise thermometer with one of the sense resistors of figure 1 replaced by the Josephson junction arrays of the QVNS and impedance-matching resistors.

Note that the uncertainty is zero if the amplifier noise is zero. If the QVNS and thermal noise powers are averaged over the same interval, τ, the relative variance in the temperature measurement is the sum of the variance with the QVNS and the variance with a thermal noise source:

$$\frac{u^2(\hat{T})}{T^2} = \frac{2}{\tau_I \Delta f_c}\left[\left(1+\frac{\langle V_{n1}^2\rangle}{\langle V_T^2\rangle}\right)\left(1+\frac{\langle V_{n2}^2\rangle}{\langle V_T^2\rangle}\right)\right], \quad (18)$$

where $\tau_I = 2\tau$. Note that the uncertainty is slightly less than for the relative primary JNT, (11).

The use of the QVNS has several major advantages for absolute primary thermometry in addition to making the direct link to quantum-based electrical standards via the fundamental constants k and h:

- The mean squared voltage noise generated by the QVNS can be programmed, and synthesized with perfect linearity, to match the thermal noise power at any temperature to minimize the effects of correlator non-linearity.
- The distribution of the voltages can be programmed to match a Gaussian distribution. This is important because the various distortion products at the output of the correlator correspond to the statistical moments of the combined distributions for the amplifier noise and QVNS waveform, or the amplifier noise and thermal noise. To properly balance the effects of non-linearity, it is necessary to match all moments of the QVNS waveform and the thermal noise distributions, not just the variances (see [59] and section 5.1.4 for detail.)
- The source impedance of the QVNS can be independently matched to the resistance of the sense resistor, enabling a close match of the frequency response of the system to signals from the resistor and the QVNS, leading to a greater bandwidth and lower uncertainty.
- The reference noise power can be changed independently of any other influence variable to investigate the effects of correlator non-linearity.
- The reference noise can be set to zero, without changing any other influence variable, to investigate the effects of electromagnetic interference (EMI).

Noise thermometers using a QVNS generating a broadband Gaussian noise have been demonstrated at NIST [20, 21] and NIM [22, 62]. Other types of traceable electrical reference sources are described by Callegaro [64] using a transformer to couple a pseudo-random Gaussian reference signal into the sensor circuit. At NMIJ [24, 65] a JNT using a superconducting pseudo-random binary sequence (PRBS) generator as the reference noise source was demonstrated. Unfortunately, the PRBS produces a reference signal with a binomial voltage distribution, rather than a Gaussian distribution, with the consequence that the measurement is more sensitive to correlator non-linearity.

2.6. Frequency-domain correlation

The preceding analysis assumes that the correlation is performed by multiplying the voltages in the time domain. However, digital signal processing and frequency-domain analysis offer several compelling advantages and, in fact, are essential if the measurements are to be auditable.

Digital measurements of noise power carried out in the time domain can be evaluated as the mean of the product of the many pairs of samples of V_1 and V_2, the voltages at the input of the two ADCs of figure 3:

$$\overline{V_1 V_2} = \frac{1}{N}\sum_{i=1}^{N} V_1(t_i)\, V_2(t_i), \quad (19)$$

where t_i are the sampling times.

For processing in the frequency domain, the two sequences of voltage samples are transformed by fast Fourier transform (FFT), $V_1(t_i) \Leftrightarrow v_1(f_j)$, and $V_2(t_i) \Leftrightarrow v_2(f_j)$, where f_j are the centre frequencies of each FFT bin. To enable the FFTs and the digital signal processing to be carried out in near-real time, the FFTs are performed on subsets of the data taken over short periods of about 1 s (during which the next block of samples is acquired). In this way, the total number of samples, N, is compiled as $N = N_1N_2N_3N_4$, where N_1 is the number of samples gathered in each FFT block of about 1 s, N_2 is the number of

FFT blocks in each 'chop' (during which the switch position in figure 3 is fixed, typically for 100 s), N_3 is the number of pairs of chops per day (giving equal numbers of measurements of the thermal noise and the QNVS noise), and N_4 is the number of days the JNT is operating. The cross-correlation operation in the frequency domain is performed on corresponding pairs of FFTs, to give a cross spectrum, which is typically averaged over a day to give a daily average cross spectrum:

$$\overline{v_1 v_2}(f_j) = \frac{1}{N_2 N_3} \sum_{i=1}^{N_2 N_3} \mathrm{Re}\left[v_1(f_j)\, v_2^*(f_j)\right], \quad j = 1..N_1/2, \tag{20}$$

where the * represents complex conjugation. The sampling frequency and length of the FFT blocks should be chosen so that N_1 is a power of 2 to allow the use of the fastest FFT algorithms. Additionally, the sampling frequency and FFT block length may be chosen to make the width of each FFT bin a convenient value, such as 1 Hz exactly.

It is also useful to compute the autocorrelation for each of the two voltages, V_1 and V_2, e.g.

$$\overline{v_1^2}(f_j) = \frac{1}{N_2 N_3} \sum_{i=1}^{N_2 N_3} v_1(f_j)\, v_1^*(f_j), \quad j = 1..N_1/2, \tag{21}$$

which gives the average power spectra of the voltages at the inputs of the amplifiers, $V_T + V_{n1}$ and $V_T + V_{n2}$. This gives information required for estimating the uncertainty, (18), and provides information on the input-noise-voltage spectra of the amplifiers.

The main advantage of frequency-domain processing is the reduction in the volume of the data. For the 2017 Boltzmann constant determination, approximately 130 TB of data was acquired. The pre-processing and averaging of the data, as daily power spectra, reduced the data storage requirements by $N_2 N_3/2$, half the number of seconds of data acquired per day (about 35 000), to about 4 GB. The reduction makes data storage practical and allows post-measurement audits to ensure the data is random and uncorrupted, and allows the evaluation of different methods of analysis (section 4).

An important benefit of the spectral analysis is the ability to detect stationary, narrow-band EMI, often caused by radio and TV broadcasts, digital communications systems, security systems, and switch-mode power supplies. Broad-band and/or non-stationary noise, such as that caused by asynchronous motors and switching temperature controllers, is generally not visible in the spectra unless the interference is extreme. Although the absence of EMI effects in the spectra is not a proof of the absence of interference [66], spectral analysis is an important tool during the development and commissioning of the thermometer.

Frequency-domain processing also enables the bandwidth to be defined digitally after all the measurements have been made, simply by selecting the appropriate bins in the averaged power spectra. Calculating the ratio of the spectra eliminates the frequency response of the correlator effectively making the chosen passband rectangular, so the correlation bandwidth is maximised and the statistical contribution to the uncertainty is minimised [43]. If this technique is employed, it is important to average as much data as possible before calculating the PSD ratios to avoid a statistical bias that can be as large as several tens of millikelvin. The bias arises because [43, 67]

$$\frac{1}{M}\left[\frac{\overline{v_R^2}(f_1)}{\overline{v_Q^2}(f_1)} + \frac{\overline{v_R^2}(f_2)}{\overline{v_Q^2}(f_2)} + \ldots + \frac{\overline{v_R^2}(f_M)}{\overline{v_Q^2}(f_M)}\right] \neq \frac{\left[\overline{v_R^2}(f_1) + \overline{v_R^2}(f_2) + \ldots \overline{v_R^2}(f_M)\right]/M}{\left[\overline{v_Q^2}(f_1) + \overline{v_Q^2}(f_2) + \ldots + \overline{v_Q^2}(f_M)\right]/M}, \tag{22}$$

that is, the average of the ratios is not equal to the ratio of the averages.

3. JNT measurement system

Figure 3 shows a block diagram of the NIST and NIM absolute primary noise thermometers with the QVNS and impedance-matching resistors replacing the reference resistor of figure 1. The following subsections describe each of the blocks in detail. Any specific parameter values or features described in the text refer specifically to the NIST and NIM JNT systems.

3.1. Sense resistors

The sense resistor must meet several requirements:

- A well-defined electrical resistance with a negligible ac-dc difference.
- A low temperature coefficient of resistance.
- A flat frequency response, necessitating low parasitic inductance and capacitance, and minimal skin effect.
- A low drift in resistance over the range of operating temperatures.
- Very low extraneous noise due to $1/f$ noise, microphonics (sensitivity to vibration), and Barkhausen noise (caused by switching of magnetic domains).

Additionally, the selected value of the sensor resistance must achieve a compromise between competing random and systematic effects. In order to minimise the statistical contribution to the uncertainty (18), the resistance should be as large as practical. However, high values of resistance increase the sensitivity to the amplifier noise currents (4), and interact with the connecting leads and input capacitance of the preamplifiers to increase the mismatch in the frequency response of the two sets of connecting leads (section 3.3). For the 2017 Boltzmann constant determination, a sensor resistance of 100 Ω was chosen to minimise the systematic effects at the expense of a small increase in the uncertainty. However, a value of 200 Ω, as used in the NIST thermometer, would also have satisfied the requirements and probably have yielded a lower total uncertainty [68]. Note that the statistical contribution to the uncertainty decreases slowly in proportion to the square root of the resistance, while most of the systematic effects increase as resistance squared.

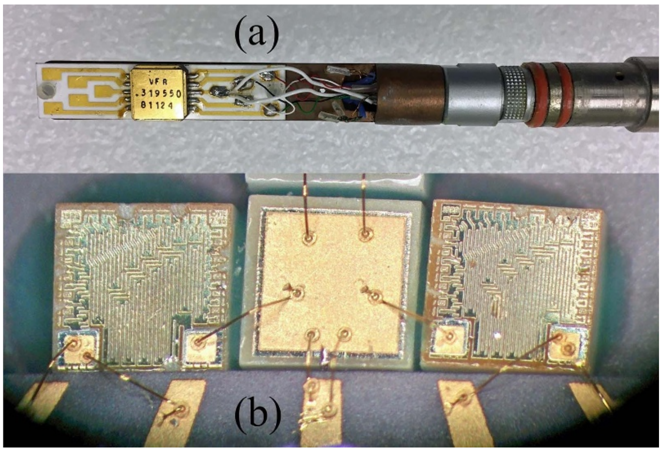

Figure 4. Photographs of the LCC sense resistor package (a) mounted at the end of the sense probe, and (b) a closeup showing the foil resistors and the grounding pad.

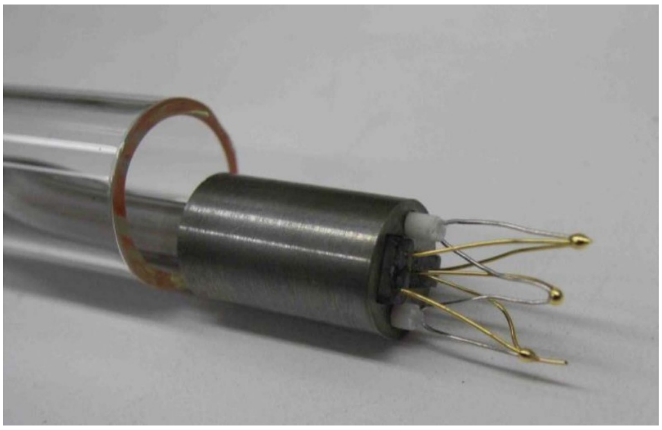

Figure 5. Photograph of a 5-wire sense resistor package mounted at the closed end of a high-temperature vitreous-silica-sheathed probe used up to 800 K. Au lead wires are welded to Pt-Rh extension wires connecting to two 50 Ω ceramic elements containing Pt-8% W alloy resistors.

3.1.1. Types for use near 273 K. The sense resistor used for all the measurements at NIST and NIM at the water triple point consists of two closely matched series-connected custom-made nickel-chrome-alloy foil resistors bonded onto a single alumina substrate (figure 4). The temperature coefficients of resistance of the resistors are less than ±5 ppm K^{-1} and the values are laser-trimmed to achieve a relative match better than 0.01% and absolute values within 0.1% of the nominal value. The foils are approximately 25 µm thick and printed with serpentine patterns over a 1.2 mm square. The serpentine pattern is designed to balance inductance and capacitance effects to provide a flat low-pass-filter like frequency dependence, extending beyond 1 GHz for resistors of about 100 Ω to 300 Ω [69]. The residual effects at low frequencies are negligible compared to transmission line mismatch effects. Four of the resistors are mounted inside a hermetically-sealed leadless chip carrier (LCC) approximately 8.9 mm square. The LCC has 10 external connections to internal gold wire interconnections that provide 4-wire definition points within on-chip wire-bonding pads. A common connection point, located along the centreline of the package, provides a common point between all the resistors that can be used as a ground point (see figure 4(b), showing two of the four resistors with five connection points). The LCC package also allows for a configuration as a four-wire short circuit in the null-measurement mode for evaluation of EMI ([70], section 5.1.5).

When the thermometer is operating, especially at temperatures above room temperature, the resistance of the sensor must be measured regularly to eliminate the effects of drift. For the 2017 Boltzmann constant determination, the resistance measurements were performed daily with an automatic direct-current comparator bridge readily achieving uncertainties below 0.1 ppm. The measurements were carried out with an excitation current of 0.25 mA to minimise self-heating.

3.1.2. Types for use above 500 K. At higher temperatures and in the presence of even small partial pressures of oxygen, the available materials and construction methods are restricted to those using glasses and ceramics for insulators, and readily welded noble metal alloys for conductors. The use of base metals in argon filled probes is usually impractical due to the difficulty of maintaining an oxygen-free environment. The sense resistors are usually wire wound elements in alumina insulators with a larger self-inductance than that of low-temperature sensors. High permeability materials may be used within the probe for magnetic shielding to attenuate EMI, but materials with a low Curie temperature may be ineffective.

Experience at NIST has shown that wire of Pt-8% W alloy is sufficiently stable in this temperature range and under low partial pressures of oxygen. The alloy has a temperature coefficient of resistance of approximately 300 ppm K^{-1}; about 1/13 of that for pure metals and yielding a change in resistance of only 9% over a 300 K interval. Although modest, the remaining temperature dependence of resistance does compromise the sensor impedance matching and the associated frequency-response matching requirements (section 3.3), perhaps necessitating different probes for different temperatures.

The parasitic reactance associated with the wire-wound resistors is larger than achievable with the foil resistors used at lower temperatures. Because reactance effects are governed by the dimensions, typically ∼10 mm or less in the resistor and ∼1000 mm or more for the connecting cables and probe, so long as the dielectric losses are small, the effects in the resistor are easily accommodated within the spectral mismatch model [21] (section 4).

Gold lead wires (figure 5) are preferred for high-temperature probes for their low resistance. The use of other noble-metal lead wires in the high-temperature portions of the probe yields a higher than desirable resistance, which increases the frequency response mismatch and contributes an additional temperature-dependent and unmatched uncorrelated noise on one of the correlator inputs. The resulting noise power mismatch (section 5.1.4), especially, causes errors that are difficult to compensate.

The performance of the sensing probe is the single factor determining the upper temperature limit of absolute primary noise thermometry. Although there are examples of noise thermometers operating at temperatures above 2000 K [11], the uncertainties increase rapidly with increasing temperature due to sensor drift caused by oxidation and diffusion of contaminants, and due to the increasing conductivity of insulating materials shunting the sensing resistance and connecting leads. Experience at NIST with thermometers operating at 800 K, suggests that the useful upper limit for absolute primary noise thermometry is not very much higher, perhaps 1000 K.

3.2. QVNS

The QVNS is a Josephson-junction delta-sigma digital-to-analog converter using oversampling techniques to produce a programmed sequence of pulses clocked at 5 GHz or more [18]. It can be programmed to produce a variety of waveforms for the measurements and for diagnostic purposes. The primary benefit of the QVNS is that the voltage pulses from each Josephson junction have a quantized area $nh/2e$, where n is an integer (normally $n = 1$). These perfectly quantized pulses make the synthesized baseband voltage calculable exactly from the known sequence of pulses, the clock frequency of the pulse generator, and the defined constants e and h.

The synthesis technique underlying the QVNS was originally developed for ac voltage standards [18]. However, the low voltages of noise thermometry necessitate a specialised QVNS with fewer junctions (typically $N_J = 8$–256) configured as a pair of symmetric grounded arrays to provide a differential signal (figure 3). Each of the arrays is separately biased with a repeating pulse drive sequence that is clocked at half the 10 GHz sampling frequency, f_s. To reduce inductive voltage errors caused by low-frequency drive currents passing through the inductive arrays, each drive pulse comprises a negative half-pulse followed by a full positive pulse followed by another negative half-pulse. This composite pulse forces each junction to generate a single output pulse, as required, while ensuring the drive waveforms have minimal low-frequency content [61].

The typical drive sequence, M composite pulses long, is generated using a delta-sigma analog-to-digital conversion algorithm programmed to produce the desired waveform. For JNT, the waveform comprises a series of sinusoids at the odd harmonics f_1, $3f_1$, $5f_1$,…, of the pattern repetition frequency, $f_1 = f_s/M$ (90 Hz). The sinusoids all have the same amplitude but random relative phases to give the waveform a Gaussian amplitude distribution, and therefore ensure the distortion products for the QVNS waveform match the distortion products for the thermal noise of the same amplitude [59].

The odd harmonic sequence is chosen to ensure that the lowest-order distortion products, which are all even order, do not fall in the FFT bins containing the tones and thereby bias the measured amplitudes of the tones of the reference signal. Figure 6 shows the calculated spectrum of a QVNS frequency comb spanning a frequency range up to 4 MHz [58]. Note that the spectrum of the digitisation by-products

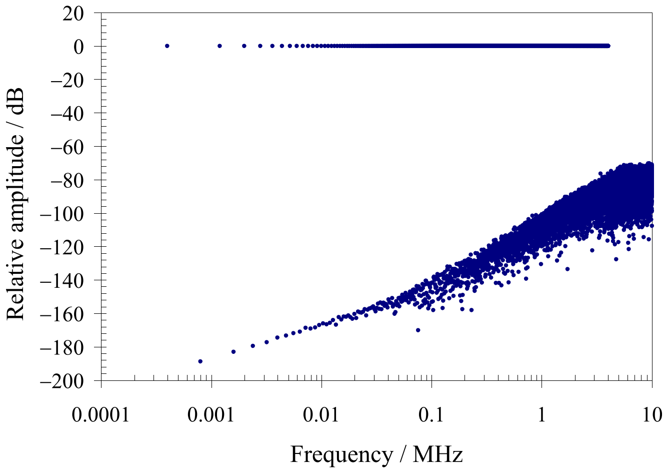

Figure 6. A QVNS output spectrum calculated from the code sequence [59]. The upper branch (up to 4 MHz) shows the odd harmonics, and the lower branch shows the even harmonics (below 4 MHz and both even and odd above that). The amplitudes of the even harmonics are indicative of the magnitudes of the errors in the amplitudes of the odd harmonics at the same frequency. Reproduced from [59].

(even harmonic tones below 4 MHz) in the generated waveform has been shaped to provide the highest accuracy at low frequencies.

The tone spacing for the JNT waveform should be as small as practical and is typically limited by the available memory in the pulse code generator since the pattern repetition frequency, $f_1 = f_s/M$ and the tone spacing is $2f_1$. A wide tone spacing means the tone amplitudes are proportionally larger for the same nominal PSD, and the intermodulation distortion products very much larger (as the cube for third-order products). Although the use of odd harmonics for the reference tones ensures that the even-order intermodulation products do not add directly to the measured tone amplitudes, small non-random odd-order distortion-induced variations in the tone amplitudes remain and contribute to the variance in the measured QVNS noise powers. NIST found that the intermodulation distortion becomes evident with long measurement times as a departure of the statistical uncertainty from its expected $1/\sqrt{\tau}$ dependence in (17) and (18), and ultimately limits the achievable uncertainty [58, 71]. When the absolute thermometer was used as a relative thermometer, there was a degree of cancelation of the distortion products in the relative ratio spectra [57]. But the cancellation was imperfect, and the distortion-limited variance remained after a sufficiently long integration time [71].

The output voltage of the QVNS (see figure 7) is coupled to the correlator through cables closely matching the cables to the sense resistor (section 3.3). Four impedance-matching resistors are placed on the chip in each of the four signal leads (figure 3) so that they produce only uncorrelated noise and are maintained at 4 K so that they do not unduly increase the uncorrelated noise in each channel of the correlator. Although the source impedance of the QVNS is matched using the resistors, the actual output impedance of the superconducting arrays

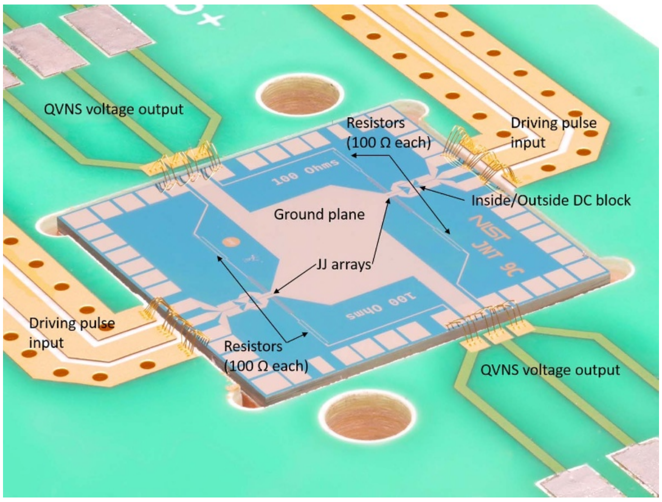

Figure 7. QVNS chip mounted on the cryogenic PCB package (composite photo courtesy of Dan Schmidt, NIST). For scale, the silicon chip (blue) is 1 cm square.

is zero, and therefore the noise currents from the preamplifiers do not generate the current related errors that occur with the purely resistive source (see (4)). This effect leads to a contribution to the PSD ratio error that increases as frequency squared and must be accommodated in the analysis (section 4.1).

With h and k defined, the only sources of uncertainty in the QNVS waveform are due to uncertainty in the clock frequency, and quantisation errors in the generated waveform. Figure 6 shows that for signals up to about 400 kHz the quantisation errors are below 1 ppm. In both the NIM and NIST systems, all clocks in the JNT system were referenced to an atomic clock, ensuring that frequency errors are below 0.01 ppm.

3.3. Connecting leads

Equation (16) for the measured temperature obscures a problem. The thermometer does not directly measure the noise voltages produced by the two noise sources. Instead, it measures the voltages after transmission through the connecting leads and switch unit to the inputs of the preamplifiers. Although the connecting leads are less than two metres long, the differences in the impedances of the two sets of leads causes measurable differences in the frequency response of the thermometer to the two noise sources. While the spectral mismatch makes only a modest direct contribution to the total uncertainty, it has a much greater indirect effect on the uncertainty by constraining the bandwidth of the thermometer, and by requiring the use of a more complicated spectral model in the analysis of the data [62] (see section 4.1). There are several causes of spectral mismatch to be considered [72].

Figure 8 shows a simplified model of the two noise sources and the connecting leads. Each model includes the noise sources and their resistances, a pi-section lumped-parameter model of the connecting leads (i.e. a 'transmission line'), and a capacitor representing the input capacitance of the preamplifiers and switch. Each model is symmetric about the noise source, and the subscripts Q and T on the variable names indicate the noise source with which the parameters are associated. An algebraic analysis of the model shows very quickly that the frequency responses of the two sets of leads are identical if and only if $R_Q = 2R_T$, $C_Q = C_T$, and $L_Q = L_T$. That is, the effective source resistance of the two noise sources, and the connecting cables to the two sources should be identical.

One of the complications of making the two sets of transmission lines identical is the need to immerse portions of the lines into different thermal environments. The QVNS transmission line has a rigid portion immersed into liquid helium while the line for the sense resistor has a separate and different rigid section (the 'probe') immersed into an isothermal zone at the temperature of interest. The difference in the temperatures of the conductors causes a difference in the electrical conductivity, and therefore also the skin effect, the distribution of ac currents, and the line inductance. At low frequencies, where the skin effect is negligible, currents are distributed uniformly through the conductors, while at high frequencies, the currents are confined near the surfaces of the conductors. In conventional coaxial cables, the inductance may change more than 15% between low and high frequencies. Thus, temperature alters the frequency dependence of the inductance of the cables and causes a mismatch in the frequency response to the two noise sources. The effect is minimised by using very fine coaxial cables with conductors made from a material with a low temperature coefficient of resistance. The use of a foam dielectric also reduces the sensitivity of the cable capacitance to temperature changes. In the NIM system, all the leads are 0.86 mm OD solid-conductor Be-Cu coaxial cables with a polytetrafluoroethylene (PTFE) foam dielectric. This choice of cable reduced the impedance mismatch by a factor of more than 20 and moved the transition between low frequency and high frequency behaviour of the cables from a few tens of kilohertz to about 200 kHz [72].

In earlier versions of the NIST and NIM thermometers, attempts were made to match the frequency response of the two sets of leads by adding discrete resistors, inductors, and capacitors at the input to the switch [58, 62]. There are two reasons why this technique fails and can in fact make the mismatch worse. Firstly, the values of the added components were selected to make the ratio of the sensor and QVNS spectra as close to unity as practical. However, the ratio of the two spectra should not be unity because the thermal spectrum includes errors due to the amplifier noise currents (4), which increase as frequency squared, and the QVNS spectrum does not. Secondly, the addition of components necessarily increases the complexity of the two frequency responses, and although the match at low frequencies might be improved, the remaining mismatch tends to have a more complicated structure and deteriorates more quickly at higher frequencies, potentially limiting the usable bandwidth. The more complex frequency response may necessitate a more complex model in the analysis, which also increases the uncertainty (see section 4).

Care must also be taken with the grounding and shielding of the sensor and its connections to minimise EMI and ensure that all impedances are well defined. For dc measurements, a 4-wire connection to the resistor is sufficient to properly

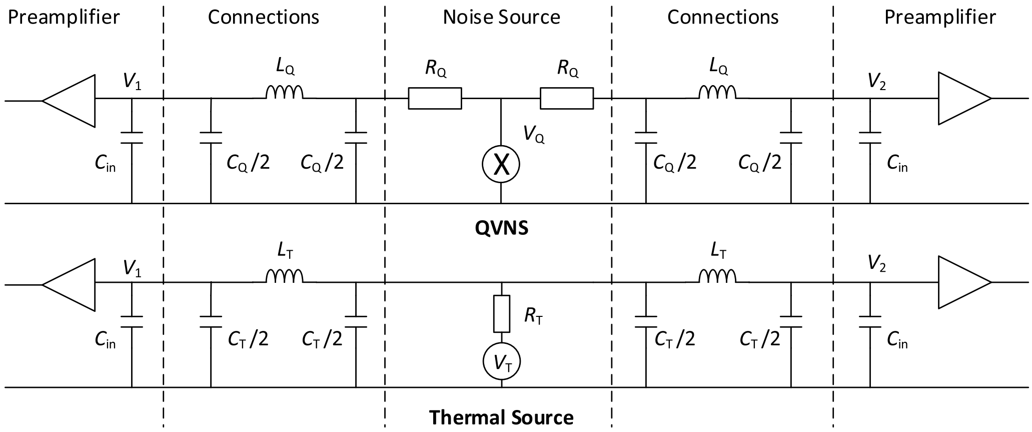

Figure 8. Model of the connections between the noise sources and preamplifiers including the pi-section model for the connecting leads and switch [72]. Reproduced from [72].

define the electrical resistance. However, with ac measurements, the impedances of the sensor and lead wires are modified by anything that interacts with the electromagnetic fields around them. The solution is to exploit the coaxial technique used in ac electrical metrology (see [73], ch 3). In a coaxial network, each conductor in the elemental circuit becomes the central conductor in the coaxial network, while the outer conductor of the network forms a single low-potential surface surrounding the entire network ensuring zero electric field outside the surface. Ground loops caused by nodes in the network of the outer conductors are eliminated by placing a coaxial (i.e. common-mode) choke on each loop of coaxial cable, which forces the current in the outer conductor to be equal and opposite to the current on the inner conductor. In this way, there is also no magnetic field outside the outer conductor. Since there are no external electric or magnetic fields generated by any part of a coaxial network, the network behaviour is independent of the placement of any of the components, or cables, or objects about them. The reciprocity principle also ensures the network is immune to EMI generated outside the outer conductor.

The coaxial scheme was applied as shown in figure 9. The solid black rectangles adjacent to each section of coaxial cable represent the coaxial chokes. One of the chokes for each probe is unnecessary, but to maintain symmetry, all leads have identical lengths and are accompanied by a choke mounted on the cables within the switch unit. The chokes are small high-permeability nano-crystalline toroidal cores wound with about 20 turns of the coaxial cable.

One consequence of using the coaxial technique is a possible difference between the resistance of the sensor as measured by a dc resistance bridge, and the ac resistance generating the noise. The mutual inductance of the coaxial cables combined with that of the chokes means that the resistance of the outer conductor of the network is reflected to the inner conductor. Thus, the coaxial (four-pair) ac resistance of the sensor is its 4-wire resistance plus the 4-wire resistance defined by the connection of the four outer conductors of the coaxial leads. A similar problem arises with the QVNS. That is, for both the thermal and QVNS noise sources, the low resistance connection between the four coaxial shields contributes to the

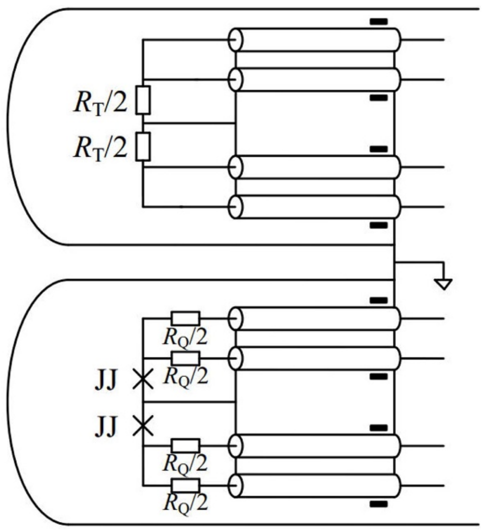

Figure 9. Schematic diagram (not to scale) showing the arrangement of the coaxial leads to the two noise sources [72]. All coaxial cables are 'grounded' at both ends. The solid black rectangles adjacent to each cable represent the coaxial chokes. Reproduced from [72].

correlated noise from the sources. For both noise sources, the junction of the outer conductors must be configured to form a 4-wire short circuit. In the NIM system, that resistance was found to be less than 1.5 μΩ, so that the relative error caused by the ac-dc difference in the resistance definitions is less than 0.02 ppm. Note that these effects also occur in non-coaxial systems, such as those using shielded twisted-pair cables, but it may be difficult to model and eliminate the effects unless a coaxial scheme is adopted.

The complications discussed here, arising from the differences in the characteristic impedances of the transmission lines, are made worse when the sense resistor probe must withstand high-temperature use. Constraints on both the materials and assembly lead to a greater impedance mismatch. In particular, complications may arise from the temperature-dependent dielectric loss in glass insulators at high temperature (see [71] and section 5.1.6 below). Details of the probe designs used at NIST up to 800 K are described in Yamazawa *et al* [71].

3.4. Switch

The function of the switch is to alternately connect the QVNS and the sense resistor to the preamplifiers. There are three important specifications for the switch. Firstly, it must be symmetric with respect to all input and output connections so that the capacitance of any input or output line does not change with the switch position. Any capacitance imbalance causes a mismatch in the frequency response of the JNT to the two noise sources.

Secondly, the switch capacitance should be as small as practical. This criterion arises, in part, because larger stray capacitances cause greater spectral mismatch effects, but also because the stray capacitance on printed circuit board (PCB) can be lossy, especially if the PCB is exposed to humid air. The dielectric loss is resistive and therefore generates a Johnson noise current that flows through the sense resistor. Ordinarily, such a noise current would not be problematic, but the noise current from dielectric losses changes with the square root of frequency, so has a distinctly different frequency dependence from most other stray noise currents, which have a linear frequency dependence [57]. If the noise current from the PCB is not negligible, then the spectral model used to analyse the data must include an additional term accompanied by an undesirable increase in the uncertainty (section 4). In the NIM thermometer, the switch was made using a PTFE circuit board rather than the more usual FR4 fibreglass PCB, and the PCB layout was optimised to ensure symmetry and the lowest practical stray capacitance.

Thirdly, the switch must not introduce any EMI into the noise thermometer. In both the NIM and NIST thermometers, the switch consists of latching relays controlled by a field-programmable gate array (FPGA). The power supply of the FPGA is turned off during the noise measurements and controlled via optical fibre to eliminate the FPGA as a source of EMI.

3.5. Preamplifiers

The preamplifiers are perhaps the most important part of the JNT and have several critical performance requirements:

- low equivalent input noise voltage to minimise the statistical uncertainty, (18),
- very low noise current to minimise the $I_n{}^2$ input-noise-current error in (4),
- low noise-current-noise-voltage correlation to minimise the V_nI_n current error in (4),
- a very high input impedance (low capacitance) to minimise spectral mismatch errors,
- good common-mode rejection ratio to minimise sensitivity to EMI.

Currently, the only preamplifier designs that meet all requirements are differential common-source-common-base cascode circuits built using discrete junction field-effect transistors (JFET) input transistors (figure 10). The preamplifier is normally operated open-loop and used as an input stage for a low-noise wide-band operational amplifier. The design requirements are discussed in detail in [50], and the circuit diagram for the NIST preamplifier given in [74]. There are some important subtleties in the design, as follows.

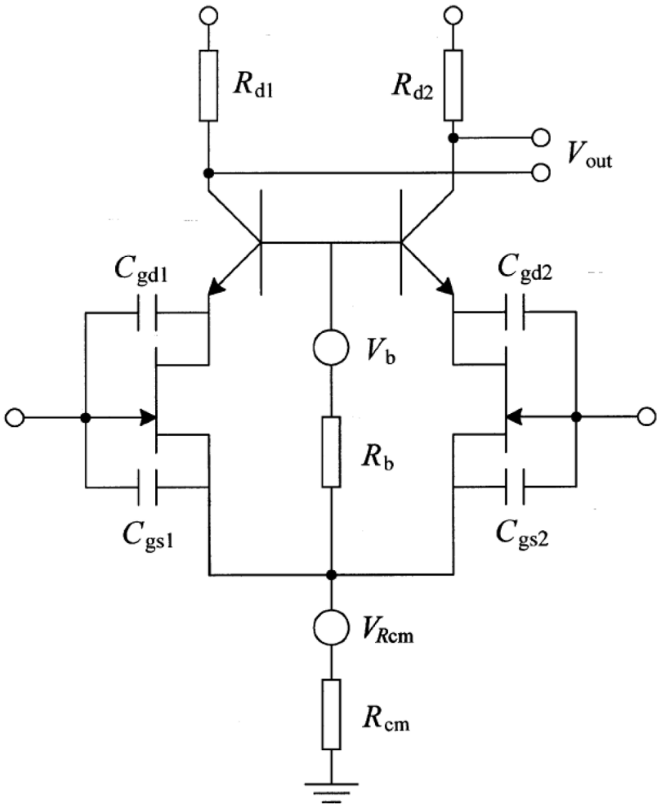

Figure 10. Schematic diagram of a differential common-source-common-base cascode amplifier.

The main source of noise in JFET is the Johnson noise current generated in the channel of the JFET. This noise is conventionally reflected to the input (gate) as an equivalent input noise voltage with a PSD,

$$S_v = \frac{\alpha 4kT_q}{G_{fs}}, \tag{23}$$

where T_q is the temperature of the carriers in the channel (normally a few degrees above the JFET temperature), G_{fs} is the JFET transconductance, and $\alpha \approx 0.7$ is a constant that depends in part on the JFET geometry [50]. The noise in the channel of the JFET is also coupled to the gate via the gate-source and gate-drain capacitances, C_{gs} and C_{gd}, giving rise to an input noise current with a PSD,

$$S_i = \frac{\alpha 4kT_q}{G_{fs}} p^2\omega^2 C_{gs}^2, \tag{24}$$

where $p^2\alpha$ takes a value between 0.1 and 0.4 depending on the JFET geometry. This noise is additional to the shot noise arising from the gate leakage current, which is usually negligible for JNT applications. Note that (24) is an empirical relation rather than a model; it includes the noise current through C_{gd}. Note too that the noise-current PSD increases as frequency squared, a feature that is exploited in the analysis (section 4). Typically, across all the different JFET geometries and families, C_{gs} and C_{gd} scale in proportion to G_{fs}, so despite appearances in (24), the noise current PSD increases in proportion to G_{fs}.

Another consequence of the proportionality between the capacitances and G_{fs} is that the product of the noise voltage and noise current densities is roughly constant, with some variation between different JFET geometries. Thus, in general, there is a 1:1 compromise between the input-noise current and the equivalent input-noise voltage. This compromise occurs also when JFETs are operated in parallel to reduce the noise voltage: the voltage noise PSD falls in proportion to the number of JFETs, while the current noise PSD increases by the same factor.

Equation (4) for the correlator error includes an error term for the noise-current-noise-voltage correlation. As implied by (23) and (24), the noise current and noise voltage share a physical cause, so a high correlation might be expected. However, the 90° phase shift between the noise voltage and the noise-current due to the passage of the current through a capacitance, means that the correlation is imaginary and, on average, zero. There are, however, aspects of amplifier design, to be discussed shortly, that cause the correlation to become real and therefore must be avoided.

The common-base cascode arrangement of figure 10 is important for two reasons. Firstly, it is necessary to minimise the Miller effect multiplication of C_{gd}, which otherwise adds significantly to the input capacitance of the preamplifier. With a high-quality cascode, the input capacitance of the differential JFET amplifier should approach $(C_{gd} + C_{gs})/2$. Secondly, a cascode with a low input resistance is necessary to minimise noise currents additional to (24). In particular, the noise currents generated in the JFET channel all appear at the JFET drain and generate a voltage proportional to the drain load impedance. Any noise voltage generated there leads to an input noise current through the gate-drain capacitance. Therefore, the impedance at the drain should ideally be zero, and a common-base bipolar transistor cascode with a low base spreading resistance is a good approximation. Note the impedance presented by the cascode should be real (i.e. a resistance). A reactive impedance causes an additional 90° phase shift in the noise currents and leads to a real correlation between the noise currents and noise voltages. Callegaro *et al* [75] describes an example of a preamplifier using an operational amplifier cascode, for which the input impedance is inductive, causing a large error in the JNT.

Another significant cause of real correlation between noise currents and noise voltages is feedback. Any feedback, local or global, causes the total equivalent input noise voltage to appear at the source of the JFET, which then leads to an additional noise current through the gate-source capacitance. Unfortunately, with feedback the voltage appearing at the source is phase shifted due to the first-order frequency dependence of the loop gain of the amplifier, which is necessary for stability. Thus, the input stage of the preamplifier should ideally be operated without any feedback. The non-linearity of the JFETs operated without feedback is not a problem because of the very small voltages involved [76].

Some care is required with the printed circuit layout to avoid common-mode Colpitts's oscillations arising from stray inductance and capacitance, including the output capacitance of the current source used to provide common-mode feedback and bias the JFETs (i.e. the tail of the 'long-tail pair'). The oscillations, which are also very common in metal–oxide–semiconductor field-effect transistors (MOSFETs) [77, 78], nearly always occur during testing when the amplifier input is shorted and are usually suppressed by resistance in the gate circuit. If oscillations occur during normal operation of the JNT, they can be suppressed using ferrite beads as common-mode chokes on the inputs to the amplifiers. Note the chokes should not be placed on individual input leads (i.e. differential mode) to the preamplifiers because of the additional inductance and high-frequency loss (noise) that will be introduced to the lead wires (section 3.3).

3.6. Bandpass filters

Because the passband of the JNT is defined digitally by selecting the appropriate FFT bins from averaged power spectra, the primary function of the bandpass filters is anti-aliasing and preventing dc overloads. The filters used in the NIM and NIST systems are passive LC-ladder filters implementing an 11th-order Butterworth response with a cut-off frequency of 1.8 MHz. With a Nyquist frequency of 2 MHz, this ensures negligible aliasing at frequencies below 1 MHz. The passive filters have several advantages compared to active filters, including the lack of a power supply, minimal susceptibility to EMI, and the elimination of the effects of amplifier distortion and overloads, all common problems with active filters.

3.7. ADCs

Perhaps the most obvious potential problems with the ADCs are quantisation error and possible correlation between the quantisation errors of the two ADCs. However, the dithering effect of both the thermal noise signal and the uncorrelated noise in each channel renders such errors negligible. So long as the rms amplitude of the uncorrelated noise is greater than one least significant bit, the relative errors in the measured noise power are below a few parts per billion [79, 80]. The dithering effects of the noise also significantly reduce the effects of differential non-linearities and other small-scale errors in the ADC characteristic so that the only important specifications for the ADC are sample rate, jitter, and integral non-linearity.

Some care is required in the operation of the ADC. To avoid clipping, the ADC should be operated with the rms noise voltage below about 1/5 of full-scale. Also, it is important that the trigger signals for the two ADCs are closely synchronised.

Both the of the NIST and NIM ADCs have 16-bit resolution and sample at 4 MHz to give a 2 MHz Nyquist frequency. The ADCs are clocked and triggered externally via optical fibres, with the phases of the clocks carefully adjusted so that the two correlator channels are closely synchronized. To ensure that the QVNS tones appear in a single FFT bin, the ADC clocks are locked to the same atomic frequency reference as the QVNS clock.

3.8. Shielding, grounding, and power supplies

EMI is perhaps the most troublesome source of error in JNT. EMI coupling into both channels results in a systematic error in the noise power measurement, and in extreme cases may induce amplifier overloads. EMI is usually unavoidable in industrial environments where the electromagnetic fields due to large electrical machines are large and uncontrolled [11].

To minimise EMI effects, all the electronic building blocks of the JNTs should be housed in metal cases and have separate power supplies powered by rechargeable batteries. This eliminates the possibility of correlated EMI originating in shared supplies, and crosstalk due to shared power supply lines.

Additionally, in the NIM and NIST thermometers, all digital signals are transmitted via optical fibre cables, and all analog signals are transmitted via short lengths of coaxial cable or shielded twisted pair. All the electronic building blocks are housed in thick-walled aluminium cases, and then enclosed in a single mu-metal case. To eliminate ground loops, only the ground of the pulse generator driving the Josephson junctions through microwave cables is directly connected to the earth point. The measurements at NIM were additionally carried out in an underground screened room distant from large electrical machinery.

Direct measurements of EMI using dummy sensing probes, explained in (section 5.1.5), provides a means of estimating the uncertainty due to EMI, and spectral analysis (section 2.6) may help identify the source of the EMI.

3.9. Signal processing

3.9.1. Real-time pre-processing. Once each of the signals from the two correlator channels have been sampled, the FFTs are computed. For the NIM and NIST systems, this yields 2 MHz wide complex spectra with 1 Hz-wide FFT bins. The complex frequency-domain cross correlation of the spectra and the autocorrelation spectra for each channel are also computed. These spectra are then accumulated over one day into an average spectrum ensuring compact data storage. When the noise source is switched, the process is repeated so that six averaged spectra are slowly accumulated. These computations are carried out in real time, during the 1 s interval that the ADCs acquire the next block of data.

3.9.2. Post processing. After the averaged spectra have been accumulated for a suitable period, usually one day, further processing occurs. First, because the QVNS spectrum has tones located only every 180 Hz, and zero elsewhere, it is not possible to calculate a direct ratio of the thermal noise and QVNS spectra. Instead, for both spectra, the noise powers in the FFT bins are summed in 180 Hz blocks centred on each of the QVNS tones, yielding an additional 180 $\times$ reduction in storage requirements and the same reduction in the variance of the noise powers in the FFT bins.

Secondly, the thermal noise spectra are corrected to account for the slow drift in the dc resistance of the sense resistor by normalising each spectrum to a nominal resistance. A reasonable approach is to multiply each daily spectrum by the ratio of the mean sensor resistance divided by the sensor resistance on the day of the measurement. The mean resistance is then used to calculate the temperature (see (14) and (16)).

4. Analysis

The post-measurement analysis of the data is one of the most important aspects of the operation of the noise thermometer. Section 3.3, discussing the differing frequency responses of the transmission lines to the two noise sources, identified a difficult compromise between the uncertainty due to the nature of the noise, which decreases with increasing bandwidth, and the uncertainty due to the spectral mismatch errors, which increase rapidly with bandwidth. This section further explains the nature of the compromise and the analysis yielding a minimum uncertainty solution to the problem.

4.1. Spectral model

Figure 11, from [22], shows a plot of the grand average of the ratio of the thermal and QVNS spectra taken over 120 d and after post processing. The plot shows a strong quadratic frequency dependence, in part due to the frequency-dependent preamplifier input-noise current (24) contribution to the measured noise power (4) from the sense resistor, and in part due to the mismatch in the frequency response of the connecting leads to the resistor and QVNS sources. The noise-induced variations in the ratios are not visible on the scale of this plot.

If the effects of noise currents due to dielectric loss (which have a PSD proportional to frequency) are assumed to be negligible, and the various stray inductances and capacitances are modelled by lumped parameters, the PSD models for the measured QVNS and thermal noise signals comprise only even-order terms in frequency. Therefore, the ratio of the two PSDs can also be modelled by the even-order power series:

$$\frac{S_R(f)}{S_Q(f)} = a_0 + a_2 f^2 + a_4 f^4 + a_6 f^6 + \dots. \tag{25}$$

Here, a_0 is the low-frequency limiting value of the PSD ratio needed to determine the temperature, (16), and the coefficients $a_2, a_4, a_6, \dots$ characterise the spectral mismatch errors.

4.2. The bias-variance trade-off

In principle, it is a simple matter to perform a least-squares fit of the model to the data of figure 11 and determine a value for a_0. But how many terms of (25) should be included in the fitted model, and what frequency band of data should be used?

The method of ordinary least squares (OLS) determines values for model parameters by minimising the sum of the squared residuals—the differences between the model and data. Typically, the sum of the squared residuals steadily decreases with increasing model complexity, as does the

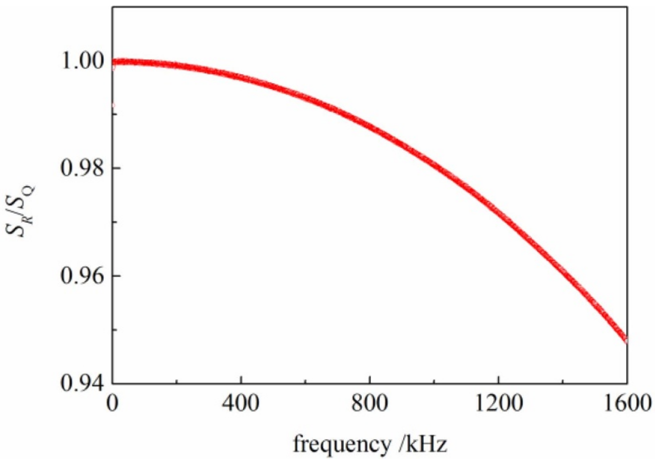

Figure 11. The ratio of the thermal and QVNS cross-correlation spectra resulting from the 120 d of measurements [22]. Reproduced from [22].

magnitude of any bias in model parameter values e.g. due to remaining unmodelled spectral mismatch errors. However, overly complex models suffer from overfitting where the fitted values of the parameters in the model become increasingly influenced by random error rather than real trends in the data, leading to a fitted model with poor predictive performance evident from an increasing variance in predicted values [81]. Note too, other systematic effects may produce non-negligible errors in a_0 and other parameters, besides the systematic effect assocaited with fitting an insufficiently complex model. In general, models with the best predictive performance still make biased predictions, and models with low prediction error may have large errors in individual parameters.

The analysis of the power spectral ratios of figure 11 has additional considerations. First, the uncertainty in the fitted value of a_0 due to the intrinsic random effects of the noise falls in proportion to the square root of the bandwidth, (18), suggesting a benefit in selecting data from a wide bandwidth. At the same time, the biasing effects of spectral mismatch errors increase at a much faster rate, proportional to f^4 or higher, suggesting a more complicated model and a lower bandwidth might be preferred.

Finally, the measured power-spectra ratios span a range of frequencies from 10 kHz (lower frequencies are omitted to avoid EMI) to several 100 kHz, so the determination of the value of a_0, from which the temperature is estimated, is an extrapolation of the model to zero frequency, and extrapolation means the uncertainty in the predicted value of a_0 increases as the model complexity increases.

So, we have a two-dimensional optimisation problem: in additional to selecting an appropriate model, we must also select an appropriate bandwidth.

4.3. Cross Validation

Cross validation (CV) is an objective (data driven) statistical technique used to evaluate the quality of a fitted model, including the model's predictive performance. It is a key tool for model selection in machine learning and statistics [81–84].

In k-fold CV, the data is partitioned into k equal-sized 'folds'. Initially, the first fold is chosen as the validation data set, while the $k-1$ remaining folds are the training data set. Each candidate model is fitted to the training set (i.e. validation data excluded) and used to predict values in the validation set. For each model, the mean squared deviation between the prediction and the validation data is determined. The process is repeated for each of the k distinct ways of defining the training and validation sets, and the mean of the k mean squared deviations calculated for each model. The results are then used to select the best performing model.

In Monte Carlo cross validation (MCCV), as employed here, the data is repeatedly and randomly partitioned into the k folds and the CV performed in k distinct ways, as described above. For each partition, the model with the lowest mean squared deviation is identified. From many random partitions, a selection fraction for each candidate model is determined and the best model identified. Although computationally more expensive than CV, MCCV has a greater probability of selecting the best model [85–87]. Additionally, as Coakley and Qu showed [88], the model selection fraction determined by MCCV can be used to determine an uncertainty accounting for both the random measurement errors and model ambiguity effects.

Below, we briefly outline the 5-fold MCCV analysis applied to the 2017 Boltzmann constant determination [22]. The method is described in detail in [88] where it is applied to data from the 2015 Boltzmann constant determination [62].

The data shown in figure 11 is the average of the PSD ratios for the 120 d that the measurements were performed. The following operations were performed.

1. Select a frequency band between 10 kHz to a maximum frequency ranging from 200 kHz to 1 MHz (in 6.25 kHz increments).
2. Partition the 120 daily average PSD ratio spectra for that band into 5 equal-sized folds.
3. Choose one of the five folds as the validation set, the remaining four are the training set.
4. Assess all models, (25) with $d = 2, 4, \ldots, 14$, using OLS and the mean of the squared prediction errors as the measure of performance.
5. Return to 3 and select a different fold as the validation fold.
6. Once each partition has been used in the five possible ways, calculate the overall mean-square prediction errors for each model and identify the best performing model. A score of 1 point is assigned to that model.
7. Return to 2 and perform 20 000 repeats of 2–6 using different random partitions of the data.
8. Once 20 000 repeats of Steps 2–6 have been performed, calculate the estimated selection fraction, $\hat{p}(d)$, for each model as the total score for the model divided by 20 000.
9. Use OLS to fit each model to the full unpartitioned data set for the selected frequency band and compute the estimated value of a_0 for each model, $\hat{a}_0(d)$, and the uncertainty in this value $\hat{\sigma}_{\hat{a}_0,\mathrm{ran}}$, as determined using the standard statistical method for OLS.

10. Identify and record the value of $\hat{a}_0(d)$, and the model index d, for which $\hat{p}(d)$ is the largest.
11. Calculate the weighted mean:

$$\bar{\hat{a}}_0 = \sum_d \hat{p}(d)\,\hat{a}_0(d). \tag{26}$$

12. Calculate the weighted mean of the variances:

$$\tilde{\sigma}_\alpha^2 = \sum_d \hat{p}(d)\,\hat{\sigma}^2_{\hat{a}_0,\mathrm{ran}}(d). \tag{27}$$

13. Calculate the variance:

$$\tilde{\sigma}_\beta^2 = \sum_d \hat{p}(d)\left(\hat{a}_0(d) - \bar{\hat{a}}_0\right)^2. \tag{28}$$

14. Calculate and record the total variance:

$$\hat{\sigma}_{\mathrm{tot}}^2 = \tilde{\sigma}_\alpha^2 + \tilde{\sigma}_\beta^2. \tag{29}$$

15. Return to 1 and select the next band of data.
16. Once the data for all the frequency bands have been evaluated, select the frequency band yielding the lowest uncertainty recorded at Step 14, the corresponding value of $\hat{a}_0(d)$ recorded at Step 10, and the corresponding uncertainty recorded at Step 14. These are the reported values.

Figure 12 shows a summary of the analysis for the 2017 Boltzmann constant determination. Figure 12(a) shows the order of the selected model versus the maximum frequency for each frequency band, 12(b) shows $\hat{\sigma}_{\mathrm{tot}}$ for the selected model, and 12(c) shows estimated values of a_0 and its standard uncertainty, for each frequency band and selected model. In 12(c), the values of a_0 are expressed as an offset relative to $a_{0,\mathrm{calc}}$, the value of a_0 calculated from the 2014 CODATA value of the Boltzmann constant [22].

There are several notable trends in figure 12. Firstly, the model complexity (figure 12(a)) yielding the lowest uncertainty generally increases with increasing frequency, as expected. Secondly, also as expected, the uncertainty associated with a single model generally falls slowly with increasing frequency. Thirdly, the estimates of the value for a_0 are remarkably consistent across all models and frequency bands, and are everywhere within one standard deviation of $a_{0,\mathrm{calc}}$, i.e. consistent with the 2014 value of the Boltzmann constant. The point corresponding to the second-order model and a maximum frequency of 368.75 kHz (bandwidth = 358.75 kHz) yields the lowest uncertainty, $\hat{\sigma}_{\mathrm{tot}}$, of 2.58 ppm.

4.4. Uncertainty considerations

The uncertainty analysis presented as (26) to (29) is based on a mixture distribution, constructed as follows. For each $f_{\max}$, for each spectral-mismatch model, OLS is used to estimate a_0, its uncertainty, $\hat{\sigma}_{\hat{a}_0,\mathrm{ran}}$, and its associated sampling distribution, which is assumed to be normal. The mixture distribution is the weighted sum of the sampling distributions for all candidate models with weights $\hat{p}(d)$, estimated using the CV. The uncertainty, $\hat{\sigma}_{\mathrm{tot}}$, is the standard deviation of the mixture model pdf. See [88–91] for more detail.

Note that $\tilde{\sigma}_\alpha^2$ is the weighted average of the estimated conditional variances of the observed a_0, and $\tilde{\sigma}_\beta^2$ is the weighted mean square deviation of the estimated conditional means of the sampling distributions from the estimated mean for the mixture, $\bar{\hat{a}}_0$. Both $\tilde{\sigma}_\alpha$ and $\tilde{\sigma}_\beta$ include the statistical effects of the noise and spectral mismatch errors. A more informative breakdown of the uncertainties is obtained by recognising that the contribution of statistical uncertainty in the estimated a_0, is estimated as $\hat{\sigma}_{\hat{a}_0,\mathrm{ran}}$ determined by OLS, and therefore the contribution of spectral-mismatch model ambiguity at the selected frequency is

$$\hat{\sigma}_{\mathrm{model}} = \left(\hat{\sigma}_{\mathrm{tot}}^2 - \hat{\sigma}^2_{\hat{a}_0,\mathrm{ran}}\right)^{1/2}. \tag{30}$$

There are additional uncertainties arising from imperfections in the bandwidth selection method. First, the MCCV was carried out at intervals of 6.25 kHz rather than a continuum of frequencies. Second, there are random fluctuations in $\hat{\sigma}_{\mathrm{tot}}$, due to several effects, that vary with fitting bandwidth. Third, different values of $f_{\max}$ can yield very similar values of $\hat{\sigma}_{\mathrm{tot}}$ but different values for the selected $\hat{a}_0$. We estimate the component of uncertainty due to bandwidth ambiguity, $\hat{\sigma}_{f_{\max}}$, as the standard deviation of the estimates of a_0 associated with the lowest 10% values of $\hat{\sigma}_{\mathrm{tot}}$, see [88] for detail.

5. Uncertainty budget

Because all the variables in equation (16) for the temperature appear as multiplying or dividing factors, the propagation of uncertainty equation is most easily expressed in relative form:

$$\frac{u^2_{T,\mathrm{total}}}{T^2} = \frac{u^2\left(S_R^2/S_Q^2\right)}{\left(S_R^2/S_Q^2\right)} + \frac{u^2\left(f_\mathrm{S}\right)}{f_\mathrm{S}^2} + \frac{u^2\left(X_R\right)}{X_R^2}, \tag{31}$$

to which must be added any uncertainty associated with the realisation of the temperature.

The uncertainty budget is summarised in table 1. The first two columns list the uncertainty components in each category identified in (31). Note that the temperature related uncertainties are specific to an experimental setup and are noted here as a reminder. The third column lists the lowest values achieved to date. These results were obtained at 273.16 K with a probe immersed into a TPW cell using a carefully adjusted measurement set up operated with environmental control and shielding from interference sources [22]. The fourth column lists values more typical of operation at higher temperatures, ∼500 K to ∼800 K, using a less optimised measurement set up [57, 71]. The higher uncertainties reflect the limitations and difficulties encountered with higher temperatures where experimental compromises are necessary, and the poorer environmental control and greater electrical interference.

5.1. Power spectral ratio S_R/S_Q

The uncertainty associated with the measurement of the ratio of the power spectral densities originates from six effects, the

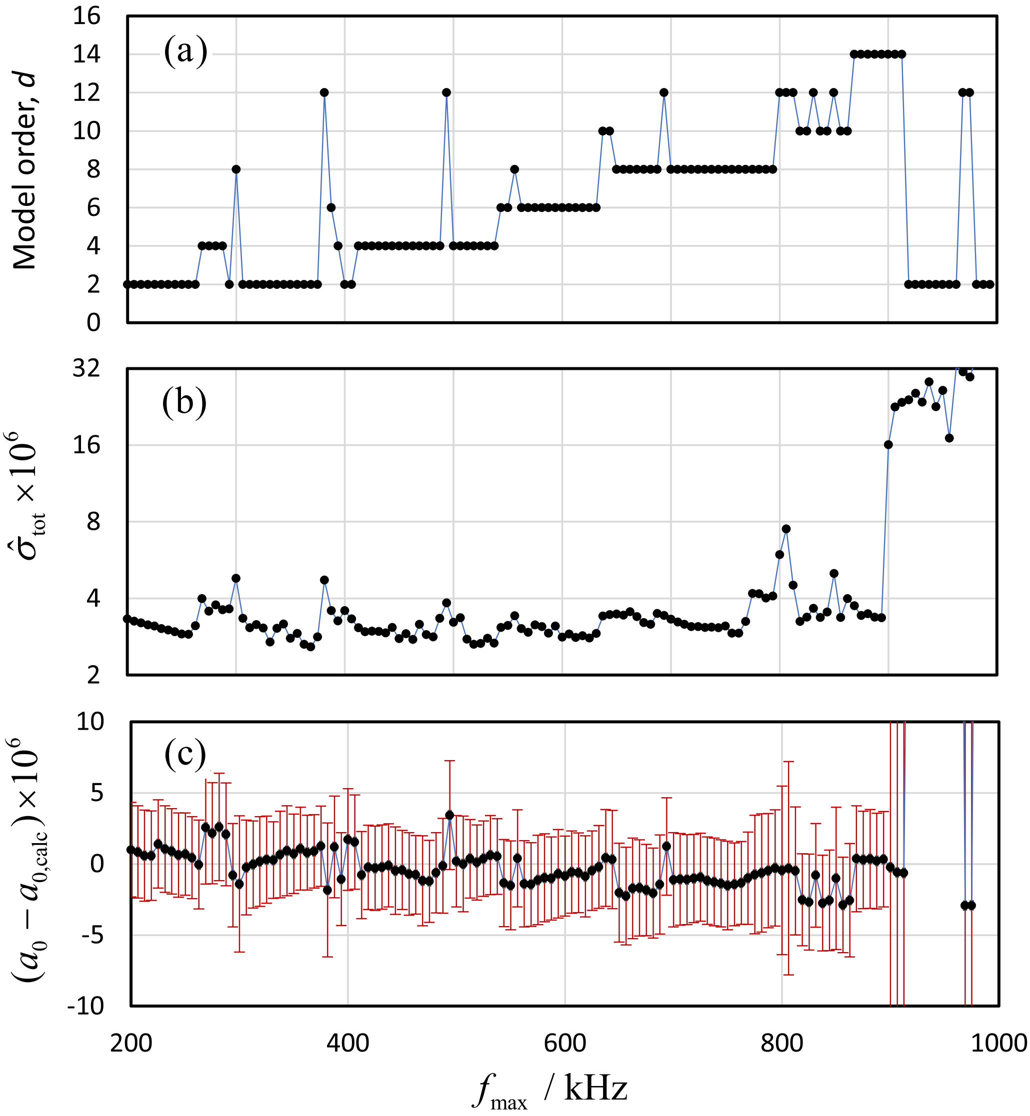

Figure 12. Results of the cross validation for each maximum frequency, $f_{\max}$ [22]: (a) the order of the most frequently selected model, d, (b) the uncertainty, $\hat{\sigma}_{\mathrm{tot}}$ (note logarithmic scale), and (c) the calculated a_0 values expressed as an offset from the a_0 value calculated using the 2014 CODATA value of the Boltzmann constant, with uncertainty bars. Reproduced from [22].

statistical uncertainty due to the random properties of the noise signals, the frequency response mismatch for the connecting leads to the noise sources, bandwidth ambiguity due to imperfections in the CV, non-linearity in the correlator, EMI, and dielectric effects, as described below.

5.1.1. Statistical uncertainty. The statistical uncertainty of the estimate of a_0 is determined by fitting the selected model to the observed data by OLS (see section 4.4)

5.1.2. Spectral-mismatch model ambiguity. At each $f_{\max}$, the component of uncertainty in the estimate of a_0 due to model ambiguity is determined from $\hat{\sigma}_{\mathrm{tot}}$ (determined by MCCV) and the statistical uncertainty determined by fitting the selected model to the observed data. See equation (30), section 4.4.

5.1.3. Frequency-band ambiguity. The contribution of imperfections in the model selection are characterised as $\hat{\sigma}_{f_{\max}}$, see section 4.4.

5.1.4. Non-linearity. To amplify the approximately 1 μV rms noise signals to a level appropriate for the ADCs, the gain in each channel of the correlator must be on the order of 10^5. Inevitably, the non-linearity in the various amplifiers, filters, and ADCs accumulates to introduce a significant error in the noise-power measurement.

A study of the various causes and effects of non-linearity [76] concluded that the causes were so numerous, and the effects so variable, that a detailed physics-based model of the non-linearity is not practical. Instead, any model of the non-linearity must be empirical and based on measurements made with deliberate changes in the noise power. One of the advantages of a noise thermometer operating with a QVNS is that it is possible to change the QVNS voltage without changing any of the other operating conditions of the JNT, and thus making non-linearity measurements practical.

Suppose the (voltage) transfer function for channel 1 of the correlator, when referred to the correlator input is represented as the Taylor series

$$V_1 = \sum_{i=1}^{\infty} a_{1,i} (V + V_{n1})^i, \quad a_{1,1} = 1, \tag{32}$$

where V is the voltage to be measured (either the V_R from the sensor or V_Q from the QVNS), the index i indicates the polynomial order of the distortion coefficient, and $V_{n,1}$ is the equivalent input noise voltage for channel 1 (a similar equation applies to channel 2). The coefficient $a_{1,0}$ therefore represents the offset voltage, and $a_{1,1}$ represents the linear gain, assumed to be equal to 1 for the purpose of analysis. All the coefficients except $a_{1,1}$ represent unwanted non-linear terms and are assumed to be small. When the Taylor series for the two channels are multiplied and averaged, the most significant errors arise from the third order non-linearities. The ratio of the measurements of noise power is approximately [76]

$$\frac{\overline{V^2_{R,\mathrm{meas}}}}{\overline{V^2_{Q,\mathrm{meas}}}} = \frac{\overline{V^2_R}}{\overline{V^2_Q}} \left[1 + 3\left(a_{1,3} + a_{2,3}\right)\left(\overline{V^2_R} - \overline{V^2_Q}\right) \right. \\ \left. + 3a_{1,3}\left(\overline{V^2_{n1,R}} - \overline{V^2_{n1,Q}}\right) + 3a_{2,3}\left(\overline{V^2_{n2,R}} - \overline{V^2_{n2,Q}}\right)\right], \tag{33}$$

so that the error due to non-linearity is zero if (i) the measured noise powers $\overline{V^2_R}$ and $\overline{V^2_Q}$ are matched, and (ii) the lead resistance and amplifier noise power for channel 1 is the same during both measurements, and (iii) the lead resistance and amplifier noise power for channel 2 is the same during both measurements. If the analysis is extended to higher order terms, it is apparent that the various distortion products correspond to products of different moments of the noise distributions. Therefore, where (33) indicates a requirement for matching the variances, there is in fact a requirement for all moments of the distributions to be matched, and this is the rationale for ensuring the QVNS signal has a Gaussian distribution with the same variance as the thermal noise.

Equation (33) also shows that the non-linearity error in the noise power ratio should be approximately proportional to the noise-power mismatch, and therefore can be measured with several deliberately mismatched values of S_R/S_Q. The simple linear model is also consistent with the known effects of dither due to the noise, which smears out any highly localised non-linearities.

The additional measurements need only run for a day, each with much larger uncertainties than that those for the primary measurement. Figure 13 shows the variations in the measured value of k versus the degree of mismatch for the Boltzmann constant determination. The line

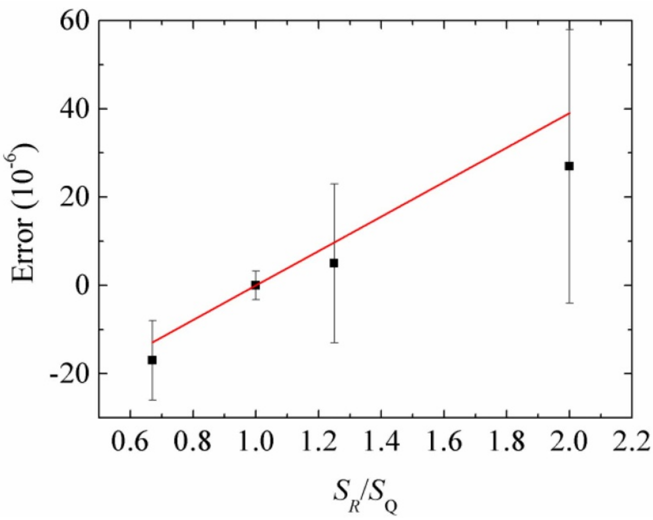

Figure 13. Estimates of the correlator error due to non-linearity of the noise thermometer versus S_R/S_Q. The red line indicates the best fit to the measured points (black squares) [62]. Reproduced from [62].

$$k_{\mathrm{meas}} = k\left[1 + \varepsilon\left(S_R/S_Q - 1\right)\right], \tag{34}$$

was fitted to the data and the non-linearity coefficient, ε, was determined to be 39 ± 20 ppm. This indicates that QVNS and thermal power spectra need only be matched to about 2.5% to reduce the effects of non-linearity below 1 ppm. With an actual match of 0.02%, the effects of non-linearity were negligible.

5.1.5. EMI. EMI is an insidious source of error. It is typically intermittent, often caused by nearby electrical machinery not associated with the JNT, and for magnetically coupled EMI at low frequencies, very difficult to shield [70, 92]. While statistical tests on the averaged spectra can detect stationary single-frequency EMI, such as caused by radio broadcasts, digital communications systems, security systems, and switch-mode power supplies, in general, spectral tests are not sufficiently powerful to detect all types of EMI [66].

Instead, evidence of the absence of EMI effects in the QVNS measurements is obtained by operating the QVNS so that it generates zero volts. Any non-zero measurement of noise power then indicates an error due to EMI. A similar test with the thermal noise source uses a 'null' thermal sensor and with the same impedance and geometric layout as the real sensor [70] forming a four-terminal zero of resistance (so that it generates zero correlated noise).

After a full day of integration, these tests have yielded residual correlated-noise powers of relative magnitude less than 0.2 ppm in both probes in a well shielded and fully isolated laboratory. A relative standard uncertainty of 0.4 ppm was assigned for possible EMI effects, since the effects may vary. Note that the uncertainties in measurements of nominal zero noise power are very much lower than for non-zero power and the measurements can be performed within a day [70]. Although the EMI measurements cannot be made concurrently with the temperature measurement, to date they appear to be the only trustworthy methods for assessing the effects of EMI.

5.1.6. Dielectric effects. Dielectric losses in any of the shunt capacitances shown in the lower diagram of figure 8 generates a noise-current that passes through the sensor resistor generating a voltage seen by both channels of the correlator and an error in the measured thermal noise power proportional to [63, 71]

$$2\pi f(-2+T_C/T)RC\tan\delta, \tag{35}$$

where R is the sensor resistance, $C\tan\delta$ is the imaginary component of the lossy shunt capacitance C, T_C is the temperature of the lossy capacitance, and f is frequency. However, the same losses do not generate a noise across the QVNS due to its extremely low (nominally zero) impedance. The asymmetry between the effects of the noise currents on the two sources introduces a small error, proportional to frequency, in the measured noise power ratio. Any fit of the spectral ratio model, (25), with a linear frequency term included results in a higher uncertainty for the a_0 term. If the term is ignored, but the actual linear contribution is significant, then an error in the OLS estimate of a_0 will result. Thus, the stray capacitance and its dielectric loss must be minimized to achieve the lowest uncertainties.

For measurements around room temperature, the best insulation materials are fluoropolymers such as PTFE and FEP due to their very low dielectric loss. Materials to avoid include nylon and some epoxy-glass composites, especially the FR4 commonly used for PCBs. Their tendency to absorb moisture combined with the high dielectric constant and electrical conductivity of water may cause a lossy and variable capacitance that depends on ambient humidity. Some variability in JNT data has been attributed to those effects [56, 57]. PCBs that contribute to the transmission line capacitances (the preamplifiers and switch) should be made from PTFE PCB, for which the loss may be an order of magnitude less than for FR4. With appropriate care, the uncertainty due to dielectric loss effects is expected to be below 0.2 ppm.

For measurements at temperatures above 200 °C or so, fluoropolymer insulation materials cease to be usable, and the best insulators are low impurity alumina ceramic and fused-silica (‘vitreous quartz’) glass. For probes employing fused silica, the OH^- impurity content is the most important factor for keeping loss tangents acceptably low [71].

5.2. QVNS waveform

The quantized nature of the voltage pulses produced by Josephson junctions in the QVNS and the very wide bandwidth of the QVNS signals ensure that the uncertainties arising from the QVNS are small. The most significant contribution arises from the digitisation noise due to the generation of a continuous baseband signal from an integer number of high-frequency QVNS pulses. The software generating the code for the QVNS exploits first-order noise shaping to push the digitisation error to the high-frequency end of the spectrum (see figure 6). The resulting error integrated over the bandwidth used in the JNT contributes no more than 0.1 ppm to the relative uncertainty.

The second source of uncertainty associated with the QVNS is the clock frequency, since that determines the frequency of the pulse train, and hence the PSD of the QVNS signal. Because the clocks for the ADCs and QVNS are all locked to the same atomic clock, the contribution to uncertainty is negligible.

5.3. Resistance

Ideally, the resistance measurements should be traceable to quantum resistance standards, therefore requiring dc measurements of the sensor resistance and a transfer standard resistance. Additional uncertainties arise from the resistance bridge, and the ac-dc difference between the dc resistance of the sensor and its ac resistance, which is responsible for the noise. Any drift observed from the daily measurements of the sensor resistance must also be assessed. For measurements near state of the art, all these uncertainties are well below 1 ppm [21].

5.4. Temperature

The uncertainty budget given in table 1 excludes explicit values for uncertainties relating to the realisation of the measured temperature because they are entirely dependent on the application, ranging from 0.1 ppm in a TPW cell to perhaps 100 ppm in a furnace at 1000 K. The values will be very different depending on the nature of the measured medium (e.g. fixed point cell, furnace, or cryostat), the probe construction, and the measured temperature. Specific factors to consider include the stability and uniformity of the zone into which the sensor is immersed, and the immersion characteristics of the sensor probe (diameter and $1/e$ characteristic length), which will behave much like industrial platinum resistance thermometers [93].

Table 1. Summary of the uncertainty budgets for absolute noise thermometry at the state of the art at 273.16 K and more typical less optimised measurements in the range 500 K–800 K.

Major component	Source of uncertainty	Uncertainty at 273 K ppm^{-1}	Uncertainty at 800 K ppm^{-1}
Ratio of the power spectral densities, S_R/S_Q	Statistical	2.37	20
	Model ambiguity	1.02	2
	Frequency band uncertainty	0.57	1
	Non-linearity	0.1	5
	EMI	0.4	10
	Dielectric effects	0.2	2
	Total $u_r(S_R/S_Q)$	2.68	23.1
QVNS waveform S_Q	Frequency reference	<0.001	<0.001
	Quantization effects	0.1	0.1
	Total (S_Q)	0.11	0.11
Realisation and equilibration of measured temperature T	Uniformity	—	—
	Stability	—	—
	Immersion effects	—	—
	Total $u_r(T_W)$	—	—
Resistance R	Ratio measurement	0.05	0.1
	Transfer Standard	0.1	0.1
	Ac-dc difference	0.1	0.1
	Relaxation and drift	0.1	1.0
	Thermoelectric effect	0.1	0.1
	Total $u_r(R)$	0.21	1.02
	TOTAL	2.7	23.1

6. Conclusion

This review collates advice on the best practice for measuring the thermodynamic temperatures with JNTs using a switched correlator and a QVNS. The best measurements to date show that absolute primary JNT can achieve a relative uncertainty in the measured temperature of about 2.7 ppm at 273 K, i.e. about 0.8 mK, with a measurement time (elapsed) of 120 d. Note that a few hours each day were dedicated to measuring the resistance of the sensor, checking the temperature realisation, and backing up data. Noise thermometers of this design are usable for temperatures as low as 4 K and as high as 1000 K, with appropriate changes in the design of the temperature sensing element, temperature probe, and preamplifiers. See [45, 57, 71] for examples of similar measurements at these temperatures.

Perhaps the most conspicuous and challenging feature of noise thermometry is the long measurement time. However, there are a few aspects of JNT operation that remain unexplored and offer possibility of improvements in measurement time and/or the uncertainty. Firstly, to date, there has been no rigorous studies determining the sense resistor value that would minimise the total uncertainty. Similarly, the preamplifier design has not been optimised for the balance between noise voltage and noise current, and there may be JFET geometries that minimise the product of these two parameters. Perhaps the most promising suggestion is to operate several noise thermometers in parallel, with the total measurement time falling with proportion to the number of thermometers.

One of the more recent developments in JNT is the superposition noise thermometer [94] where the reference noise voltage and thermal noise voltages are superimposed in one combined signal. This enables a single noise measurement to be made without the need and complications of switching inputs. Instead, the different FFT bins in the spectrum are identified as unknown or reference and the reference tones at different frequencies used to correct for the frequency response of the amplifiers, filters, and ADCs. This technique eliminates the switch, halves the number of spectral measurements (and measurement time), and enables an increased bandwidth, but it does require very high linearity of the electronics. Two separate development efforts are underway at present, one for industrial applications [94, 95], and one for primary measurements [96–98]. There remain unresolved questions about the effects of spectral mismatch and non-linearity when low uncertainties are required.

Another approach, which also exploits highly linear and stable electronics, is to simply to measure the noise power over a wide bandwidth, supported by occasional internal calibrations against a dc reference, and less frequent calibrations against a QVNS [99–102]. This method eliminates some of the concerns about non-linearities associated with the superposition method, at the expense of increased dependence on models of amplifier noise currents and voltages, and of the system frequency response. The long-term aim of the project is to meet primary metrological needs by matching the part-per-million performance of the correlator QVNS systems, but with a shorter measurement time.

ORCID iDs

Samuel P Benz https://orcid.org/0000-0002-8679-0765
Kevin J Coakley https://orcid.org/0000-0003-3787-2577
Nathan E Flowers-Jacobs https://orcid.org/0000-0002-9081-5187
Horst Rogalla https://orcid.org/0000-0003-3946-0891
Weston L Tew https://orcid.org/0000-0002-9979-9136
Jifeng Qu https://orcid.org/0000-0002-2026-9184
D Rod White https://orcid.org/0000-0002-8156-7943
Christof Gaiser https://orcid.org/0000-0003-1745-7368
Alessio Pollarolo https://orcid.org/0000-0002-7501-9289
Chiharu Urano https://orcid.org/0000-0002-7581-2009

References

[1] BIPM 2022 *The International System of Units* 9th edn (BIPM) (available at: www.bipm.org/en/publications/si-brochure/)
[2] Ripple D C, Gam K S, Hermier Y, Hill K D, Rusby R L, Steele A G, Steur P P M, Stock M, Strouse G F and White D R 2005 *Summary of Facts Relating to Isotopic Effects and the Triple Point of Water: report of the ad hoc Task Group on the Triple Point of Water* (CCT Working Document) pp CCT/05-07-07
[3] Peruzzi A and Dedyulin S 2022 NRC measurement set-up and preparatory work for CCT-K7. 2021 key comparison of triple-point-of-water cells *Metrologia* **59** 045011
[4] Dedyulin S N *et al* 2020 On the long-term stability of the triple-point-of-water cells *Metrologia* **57** 065032
[5] BIPM 2019 Mise en pratique for the definition of the kelvin in the SI (BIPM) (available at: www.bipm.org/en/publications/mises-en-pratique/)
[6] Moldover M R, Gavioso R M, Mehl J B, Pitre L, de Podesta M and Zhang J T 2014 Acoustic gas thermometry *Metrologia* **51** R1
[7] Machin G, Bloembergen P, Anhalt K, Hartmann J, Sadli M, Saunders P, Woolliams E, Yamada Y and Yoon H 2010 Practical implementation of the mise-en-pratique for the definition of the kelvin above the silver point *Int. J. Thermophys.* **31** 1779–88
[8] Saunders P, Woolliams E, Yoon H, Todd A, van der Ham E, Anhalt K, Werner L, Taubert D R, Briaudeau S and Khlevnoy B 2018 Uncertainty estimation in primary radiometric temperature measurement *Annex to the Mise en Pratique for the Definition of the kelvin* (available at: www.bipm.org/utils/en/pdf/si-mep/MeP-K-2018_Absolute_Primary_Radiometry_Uncertainty.pdf)
[9] Gaiser C, Zandt T and Fellmuth B 2015 Dielectric-constant gas thermometry *Metrologia* **52** S217–26
[10] Rourke P M C, Gaiser C, Gao B O, Ripa D M, Moldover M R, Pitre L and Underwood R J 2019 Refractive-index gas thermometry *Metrologia* **56** 032001
[11] Qu J F, Benz S P, Rogalla H, Tew W L, White D R and Zhou K L 2019 Johnson noise thermometry *Meas. Sci. Technol.* **30** 112001
[12] Klempt G 1982 Errors in Johnson noise thermometry *Temperature: Its Measurement and Control in Science and Industry* vol 5, ed J F Schooley (AIP) pp 125–8
[13] White D R 1984 Systematic errors in a high-accuracy Johnson noise thermometer *Metrologia* **20** 1
[14] Storm L 1986 Precision measurements of the Boltzmann constant *Metrologia* **22** 229–34
[15] Gallop J 2003 SQUIDs: some limits to measurement *Supercond. Sci. Technol.* **16** 1575–82
[16] Engert J and Kirste A 2019 MePK MeP-K low temperature Johnson noise thermometry *Annex to the Mise en Pratique for the Definition of the kelvinhttps* (available at: www.bipm.org/utils/en/pdf/si-mep/MeP-K-2019-LT_Johnson_Noise_Thermometry.pdf) (edition 2019)
[17] Benz S P and Hamilton C A 1996 A pulse-driven programmable Josephson voltage standard *Appl. Phys. Lett.* **68** 3171–3
[18] Benz S P, Hamilton C A, Burroughs C J, Harvey T E, Christian L A and Przybysz J X 1998 Pulse-driven Josephson digital/analog converter [voltage standard] *IEEE Trans. Appl. Supercond.* **8** 42–47
[19] Benz S P, Dresselhaus P D and Burroughs C J 2010 Multitone waveform synthesis with a quantum voltage noise source *IEEE Trans. Appl. Supercond.* **21** 681–6
[20] Flowers-Jacobs N E, Pollarolo A, Coakley K J, Fox A E, Rogalla H, Tew W L and Benz S P 2017 A Boltzmann constant determination based on Johnson noise thermometry *Metrologia* **54** 730
[21] Flowers-Jacobs N E, Pollarolo A, Coakley K J, Weis A C, Fox A E, Horst R, Tew W L and Benz S P 2017 The NIST johnson noise thermometry system for the determination of the Boltzmann constant *J. Res. Natl Inst. Stan.* **122** 46
[22] Qu J F, Benz S P, Coakley K, Rogalla H, Tew W L, White D R, Zhou K L and Zhou Z Y 2017 An improved electronic determination of the Boltzmann constant by Johnson noise thermometry *Metrologia* **54** 549–58
[23] Newell D B *et al* 2018 The CODATA 2017 values of *h, e, k*, and N_A for the revision of the SI *Metrologia* **55** L13
[24] Urano C, Yamazawa K and Kaneko N H 2017 Measurement of the Boltzmann constant by Johnson noise thermometry using a superconducting integrated circuit *Metrologia* **54** 847–55
[25] Johnson J B 1927 Thermal agitation of electricity in conductors *Nature* **119** 50–51
[26] Johnson J B 1928 Thermal agitation of electricity in conductors *Phys. Rev.* **32** 97–109
[27] Nyquist H 1928 Thermal agitation of electric charge in conductors *Phys. Rev.* **32** 110–3
[28] Einstein A 1905 Investigations on the theory of the Brownian movement *Ann. Phys.* **17** 549–60
Einstein A 1956 *Investigations on the Theory of the Brownian Movement* (Courier Corporation) (English translation)
[29] Callen H B and Welton T A 1951 Irreversibility and generalized noise *Phys. Rev.* **83** 34–40
[30] Kubo R 1966 The fluctuation-dissipation theorem *Rep. Prog. Phys.* **29** 255–84
[31] Dicke R H 1946 The measurement of thermal radiation at microwave frequencies *Rev. Sci. Instrum.* **17** 268–75
[32] Abbott D, Davis B R, Phillips N J and Eshraghian K 1996 Simple derivation of the thermal noise formula using window-limited Fourier transforms and other conundrums *IEEE Trans. Educ.* **39** 1–13
[33] Kish L B, Niklasson G and Granqvist C G 2016 Zero thermal noise in resistors at zero temperature *Fluct. Noise Lett.* **15** 1640001
[34] Reggiani L and Alfinito E 2017 The puzzling of zero-point energy contribution to black-body radiation spectrum: the role of Casimir force *Fluct. Noise Lett.* **16** 1771002
[35] Reggiani L and Alfinito E 2019 Fluctuation dissipation theorem and electrical noise revisited *Fluct. Noise Lett.* **18** 1930001

[36] Brixy H G 1971 Temperature measurement in nuclear reactors by noise thermometry *Nucl. Instrum. Methods Phys. Res.* **97** 75–80
[37] Brixy H, Hecker R, Oehmen J, Rittinghaus K F, Setiawan W and Zimmermann E 1992 Noise thermometry for industrial and metrological applications at KFA Jülich temperature *Its Measurement and Control in Science and Technology* Vol 5, ed J F Schooley (AIP) pp 993–6
[38] Fink H J 1959 A new absolute noise thermometer at low temperatures *Can. J. Phys.* **37** 1397–406
[39] Rice S O 1944 Mathematical analysis of random noise Part 1 *Bell Syst. Tech. J.* **23** 282–332
[40] Van der Ziel A 1954 *Noise: Sources, Characterisation, Measurement* (Prentice-Hall)
[41] Blackman R B and Tukey J W 1958 The measurement of power spectra from the point of view of communications engineering part 1 *Bell Syst. Tech. J.* **37** 185–282
[42] Burdic W S 1968 *Radar Signal Analysis* (Prentice-Hall)
[43] White D R, Benz S P, Labenski J R, Nam S W, Qu J F, Rogalla H and Tew W L 2008 Measurement time and statistics for a noise thermometer with a synthetic-noise reference *Metrologia* **45** 395–405
[44] BIPM 2008 Guide to the expression of uncertainty in measurement *JCGM 100:2008* (BIPM)
[45] Klein H H, Klempt G and Storm L 1979 Measurement of the thermodynamic temperature of ^{4}He at various vapour pressures by a noise thermometer *Metrologia* **15** 143–54
[46] Brixy H, Hecker R, Oehmen J and Zimmermann E 1991 Temperature measurements in the high-temperature range (1000 °C–2000 °C) by means of noise thermometry *High Temp.-High Press.* **23** 625–31
[47] White D R *et al* 1996 The status of Johnson noise thermometry *Metrologia* **33** 325
[48] Edler F, Kühne M and Tegeler E 1999 Noise thermometry above 960 °C *Proc. TEMPMEKO 1999* ed J F Dubbledam (VSL) pp 394–9
[49] Crovini L and Actis A 1975 Systematic errors in high temperature noise thermometry *Inst. Phys. Conf. Ser.* ed B F Billing and T J Quinn **26** 398–408
[50] White D R and Zimmermann E 2000 Preamplifier limitations on the accuracy of Johnson noise thermometers *Metrologia* **37** 11–23
[51] Pickup C P 1975 A high-resolution noise thermometer for the temperature range 90–100 K *Metrologia* **11** 151
[52] Edler F 2003 Thermodynamic temperature of the freezing point of copper measured by noise thermometry *Temperature: Its Measurement and Control in Science and Industry* ed Ripple D C (AIP) pp 13–18
[53] Edler F, Kühne M and Tegeler E 2004 Noise temperature measurements for the determination of the thermodynamic temperature of the melting point of palladium *Metrologia* **41** 47–55
[54] White D, Mason R and Saunders P 2001 Progress towards a determination of the indium freezing point by Johnson noise thermometry *Proc. TEMPMEKO 2001* ed B Fellmuth (VDE Verlag Gmbh) pp 129–34
[55] De Groot M, Dubbeldam J, Brixy H, Edler F, Dhupia G and Chattle M 1996 Development of a high temperature resistance thermometer using noise thermometry *Proc. TEMPMEKO P* Marcarino (Levrotto & Bell)
[56] Labenski J R, Tew W L, Benz S P, Nam S W and Dresselhaus P 2008 A determination of the ratio of the zinc freezing point to the tin freezing point by noise thermometry *Int. J. Thermophys.* **29** 1–17
[57] Tew W L, Benz S P, Dresselhaus P D, Coakley K J, Rogalla H, White D R and Labenski J R 2010 Progress in noise thermometry at 505 K and 693 K using quantized voltage noise ratio spectra *Int. J. Thermophys.* **31** 1719–38
[58] Benz S, White D R, Qu J, Rogalla H and Tew W 2009 Electronic measurement of the Boltzmann constant with a quantum-voltage-calibrated Johnson noise thermometer *C. R. Phys.* **10** 849–58
[59] White D R and Benz S P 2008 Constraints on a synthetic-noise source for Johnson noise thermometry *Metrologia* **45** 93
[60] Benz S P and Waltman S B 2014 Pulse-bias electronics and techniques for a Josephson arbitrary waveform synthesizer *IEEE Trans. Appl. Supercond.* **24** 1–7
[61] Zhou K, Qu J and Benz S P 2015 Zero-compensation method and reduced inductive voltage error for the AC Josephson voltage standard *IEEE Trans. Appl. Supercond.* **25** 1–6
[62] Qu J, Benz S P, Pollarolo A, Rogalla H, Tew W L, White R and Zhou K 2015 Improved electronic measurement of the Boltzmann constant by Johnson noise thermometry *Metrologia* **52** S242–56
[63] Benz S P, Pollarolo A, Qu J, Rogalla H, Urano C, Tew W L, Dresselhaus P D and White D R 2011 An electronic measurement of the Boltzmann constant *Metrologia* **48** 142
[64] Callegaro L, D'Elia V, Pisani M and Pollarolo A 2009 A Johnson noise thermometer with traceability to electrical standards *Metrologia* **46** 409–15
[65] Maezawa M, Yamada T and Urano C 2014 Integrated quantum voltage noise source for Johnson noise thermometry *J. Phys.: Conf. Ser.* **507** 042023
[66] Willink R and White D R 1998 Detection of corruption in Gaussian processes with application to noise thermometry *Metrologia* **35** 787–98
[67] Pollarolo A, Tew W, Rogalla H, Underwood J M and Benz S P 2014 Systematic error resolved in NIST Johnson noise thermometer *29th Conf. on Precision Electromagnetic Measurements (CPEM 2014)* pp 26–27
[68] Pollarolo A, Jeong T, Benz S P and Rogalla H 2013 Johnson noise thermometry measurement of the boltzmann constant with a 200 Ω sense resistor *IEEE Trans. Instrum. Meas.* **62** 1512–7
[69] Alpha Electronics 2020 *Ultra Precision Resistors Databook* (Alpha Electronics)
[70] White D R and Mason R S 2004 An EMI test for Johnson noise thermometry *Proc. TEMPMEKO 2004* (University of Zagreb) pp 485–90
[71] Yamazawa K, Tew W L, Pollarolo A, Rogalla H, Dresselhaus P D and Benz S P 2013 Improvements to the Johnson noise thermometry system for measurements at 505–800 K *AIP Conf. Proc.* **1552** 50–55
[72] White D R and Qu J-F 2017 Frequency-response mismatch effects in Johnson noise thermometry *Metrologia* **55** 38
[73] Awan S, Kibble B and Schurr J 2011 *Coaxial Electrical Circuits for Interference-Free Measurements* (IET)
[74] Qu J F, Benz S P, Rogalla H and White D R 2009 Reduced nonlinearities and improved temperature measurements for the NIST Johnson noise thermometer *Metrologia* **46** 512–24
[75] Callegaro L, Pisani M and Ortolano M 2010 Systematic errors in the correlation method for Johnson noise thermometry: residual correlations due to amplifiers *Metrologia* **47** 272
[76] White D R 2012 Non-linearity in Johnson noise thermometry *Metrologia* **49** 651–5
[77] Toshiba Corp. 2018 Parasitic oscillation and ringing of power MOSFETs: application note
[78] Dodge J 2004 *Application Note APT-0402 Eliminating Parasitic Oscillation between Parallel MOSFETs* (Advanced Power Technology)

[79] White D R and Pickup C P 1987 Systematic errors in digital cross correlators due to quantization and differential non-linearity *IEEE Trans. Instrum. Meas.* **36** 47–53

[80] Widrow B and Kollár I 2008 *Quantization Noise: Roundoff Error in Digital Computation, Signal Processing, Control, and Communications* (Cambridge University Press)

[81] James G, Witten J G, Hastie D T and Tibshirani R 2013 *An Introduction to Statistical Learning* (Springer)

[82] Stone C 1974 Cross-validatory choice and assessment of statistical predictions *J. R. Stat. Soc.* B **36** 111–47

[83] Stone C 1977 An asymptotic equivalence of choice of model by cross-validation and Akaike's criterion *J. R. Stat. Soc.* B **39** 44–47

[84] Arlot S and Celisse A 2010 A survey of cross-validation procedures for model selection *Stat. Surv.* **4** 40–79

[85] Picard R R and Cook R D 2004 Cross-validation of regression models *J. Am. Stat. Assoc.* **79** 575–83

[86] Shao J 1993 Linear model selection by cross-validation *J. Am. Stat. Assoc.* **88** 486–94

[87] Xu Q S, Liang Y Z and Du Y P 2004 Monte Carlo cross validation for selecting a model and estimating the prediction error in multivariate calibration *J. Chemometr.* **18** 112–20

[88] Coakley K J and Qu J 2017 Spectral model selection in the electronic measurement of the Boltzmann constant by Johnson noise thermometry *Metrologia* **54** 204

[89] Burnham K P and Anderson D R 2004 *Model Selection and Multimodel Inference: A Practical Information-Theoretical Approach* 2nd edn (Springer)

[90] Claeskens G and Hjort N L 2008 *Model Selection and Model Averaging* (Cambridge University Press)

[91] Blitzstein J K and Hwang J 2019 *Introduction to Probability* (CRC Press)

[92] Ott H W 1988 *Noise Reduction Techniques in Electronic Systems* 2nd edn (Wiley)

[93] White D R and Jongenelen C L 2010 The immersion characteristics of industrial PRTs *Int. J. Thermophys.* **31** 1685–95

[94] Bramley P, Cruickshank D and Aubrey J 2020 Developments towards an industrial Johnson noise thermometer *Meas. Sci. Technol.* **31** 054003

[95] Pearce J V, Bramley P and Cruickshank D 2020 Development of a driftless Johnson noise thermometer for nuclear applications *EPJ Web of Conf.s* vol 225 (EDP Sciences) p 03001

[96] Zhou K, Han Q, Shi Y, Wang M, Zhao J and Qu J 2020 Superposition Johnson noise thermometry with a quantum voltage noise source for calibration *2020 Conf. on Precision Electromagnetic Measurements (CPEM Digest)* (IEEE) pp 1–2

[97] Zhong Y, Zhou K, Li J, Qu J, Cao W, Wang X, Ni Z, Han Q, Zhang M and Zhong Q 2021 Fabrication and characterization of a quantum voltage noise source chip for a johnson noise thermometer *IEEE Access* **9** 113239–45

[98] Han Q, Zhou K, Shi Y, Yang J, Liang Q and Qu J 2022 Superposition Johnson noise thermometer with a fully differential structure *2022 IEEE Int. Instrumentation and Measurement Technology Conf. (I2MTC)* (IEEE) pp 1–6

[99] Kraus M, Drung D, Behr R, Palafox L, Kieler O, Bauer S and Herick J 2020 Measurement and analysis of high-frequency voltage errors in the Josephson arbitrary waveform synthesizer *Meas. Sci. Technol.* **31** 125003

[100] Drung D and Krause C 2021 Dual-mode auto-calibrating resistance thermometer: a novel approach with Johnson noise thermometry *Rev. Sci. Inst.* **92** 034901

[101] Kraus M, Drung D, Krause C, Palafox L and Behr R 2021 Linearity measurements of critical Johnson noise thermometer components with low-distortion multitones from a Josephson arbitrary waveform synthesizer *Meas. Sci. Technol.* **32** 065006

[102] Drung D, Kraus M and Krause C 2021 Calibration of the dual-mode auto-calibrating resistance thermometer with few-parts-per-million uncertainty *Meas. Sci. Technol.* **33** 015008